Annu. Rev. Biomed. Eng. 2002. 4:375–405
doi: 10.1146/annurev.bioeng.4.092101.125733

ON THE METRICS AND EULER-LAGRANGE EQUATIONS OF COMPUTATIONAL ANATOMY

Michael I. Miller
Center for Imaging Science, The Johns Hopkins University, Baltimore, Maryland 21218; e-mail: mim@cis.jhu.edu

Alain Trouvé
Université Paris 13, Institut Galilée, 93430 Villetaneuse, France; e-mail: trouve@math.univ-paris13.fr

Laurent Younes
CMLA, ENS-Cachan, 94235 Cachan Cedex, France; e-mail: younes@cmla.ens-cachan.fr

Key Words morphometrics, shape, image understanding, deformable templates, medical imaging

■ **Abstract** This paper reviews literature, current concepts and approaches in computational anatomy (CA). The model of CA is a Grenander deformable template, an orbit generated from a template under groups of diffeomorphisms. The metric space of all anatomical images is constructed from the geodesic connecting one anatomical structure to another in the orbit. The variational problems specifying these metrics are reviewed along with their associated Euler-Lagrange equations. The Euler equations of motion derived by Arnold for the geodesics in the group of divergence-free volume-preserving diffeomorphisms of incompressible fluids are generalized for the larger group of diffeomorphisms used in CA with nonconstant Jacobians. Metrics that accommodate photometric variation are described extending the anatomical model to incorporate the construction of neoplasm. Metrics on landmarked shapes are reviewed as well as Joshi's diffeomorphism metrics, Bookstein's thin-plate spline approximate-metrics, and Kendall's affine invariant metrics. We conclude by showing recent experimental results from the Toga & Thompson group in growth, the Van Essen group in macaque and human cortex mapping, and the Csernansky group in hippocampus mapping for neuropsychiatric studies in aging and schizophrenia.

CONTENTS

INTRODUCTION

Revolutionary advances in the development of digital imaging modalities combined with advances in digital computation are enabling researchers to make major advances in the precise study of the awesome biological variability of human anatomy. This is emerging as the exciting new field of computational anatomy (CA) (1, 2). CA, as first defined in Reference (2), has three principal aspects: (*a*) automated construction of anatomical manifolds, points, curves, surfaces, and subvolumes; (*b*) comparison of these manifolds; and (*c*) the statistical codification of the variability of anatomy via probability measures allowing for inference and hypothesis testing of disease states. This review will focus on aspects (*b*) and (*c*). Although the study of structural variability of such manifolds can certainly be traced back to the beginnings of modern science, in his influential treatise "On Growth and Form" in 1917, D'Arcy Thompson had the clearest vision of what lay ahead, namely:

> In a very large part of morphology, our essential task lies in the comparison of related forms rather than in the precise definition of each; and the *deformation* of a complicated figure may be a phenomenon easy of comprehension, though the figure itself may have to be left unanalyzed and undefined. This process of comparison, of recognizing in one form a definite permutation or *deformation* of another, apart altogether from a precise and adequate understanding of the original 'type' or standard of comparison, lies within the immediate province of mathematics and finds its solution in the elementary use of a certain method of the mathematician. This method is the Method of Coordinates, on which is based the Theory of Transformations.

The study of shape and structure has certainly progressed a long way; Thompson's vision is precisely the mathematical structure we term anatomy in CA (1, 2), a Grenander deformable template (3) in which the space of anatomical imagery is an orbit under groups of transformations. There are two types of transformations, the first of the geometric or shape type studied through mappings of the coordinate systems of the anatomies. Variation in the image space is accomodated by introducing groups of diffeomorphic transformations carrying individual elements from one to another. The diffeomorphic transformations (invertible differentiable mappings with differentiable inverse) fill out the anatomy. The second transformation type is of the photometric values accomodating the appearance or creation of new structures. Equally exciting is that in recent years, metric space structures have been associated with the orbits of anatomical imagery. The metric is calculated via equations of motion describing the geodesic connection between the elements. Thus the original vision of Grenander's metric pattern theory is in large part being carried out in CA: Metric distances between patterned shapes and structures are measured via distances between the mappings.

In this paper, we first describe some of the recent work in the mapping literature of computational neuro-anatomy. We then review the basic model of CA as a Grenander deformable template, an orbit generated under groups of diffeomorphisms. Next, we define metrics between anatomies associated with shortest length paths connecting one anatomical mapping to another in the orbit, measuring both geometric and photometric variation. The variational problems specifying these metrics are reviewed along with the associated Euler-Lagrange equations. Interestingly, the Euler-Lagrange equations of motion for the geodesics characterizing the metric generalize the Euler equations of Arnold (4) from flows through the group of volume-preserving diffeomorphisms to those appropriate for the more general space of non-volume-preserving diffeomorphisms appropriate for the study of general shapes. In this context, metrics on landmarked shapes are reviewed. We conclude by showing results on the study of growth and development, human and macaque cortex, and computational neuropsychiatry in aging and schizophrenia.

RECENT PROGRESS IN CA

The area of mathematical codification of biological and anatomical structure has been exploding over the past several decades. Digital electronic databases are currently available (5), especially for colocalization of volume datasets such as those encountered with PET/SPECT, CT, and MRI (6–14). Suitable atlases supporting neuromorphometric analyses (15) are now becoming available with the advent of large volumetric image data sets with large numbers of voxel samples. Complementary to the atlas development work, there has been great progress in the application of D'Arcy Thompson's transformations in cataloguing and in studying shapes. The earliest landmark and volume mapping work of biological coordinates, pioneered in the early 1980s by Bookstein (16) and Bajcsy (7), continues today in many groups including the Ayache-Gourdon-Thirion group (17–22), the Bajcsy-Gee

group (7, 8, 23–27), the Bookstein group (16, 28–33), the Dale-Fischl group (34–37), the Duncan-Staib group (38–44), the Evans group (45–53), the Friston group (48, 54, 55), our own Grenander-Miller-Trouvé-Younes group (1, 2, 56–76, 76a), the Kikinis-Jolesz group (77–82), the Davatzikos-Prince group (83–92), the Sapiro group (92a–92c), the Hurdal-Sumners group (93), the Mazziotta-Toga group (11, 94–98), the van Essen group (66, 99–101), and the Wandell group (92c, 101a, 101b), to name a few. Many of these approaches have studied higher dimensional transformations and mappings. Concurrently, efforts have proceeded along the lines of establishing the power of these approaches in lower and moderate dimensional settings in which the image structures being matched are more globally defined, with the variability of global structures being the primary goal of successful registration. Complementary to the volume work, there has been great progress on anatomical mapping via subsets of landmarked points. For such approaches, predefined subsets of the anatomy provide registration information and become the principal features about which variational studies between the various coordinate systems proceed.

Structured approaches via deformable templates and contour and surface models studying the variations of substructures via boundaries and surfaces via vector field transformations have emerged in many of these efforts. Detailed gross macroscopic studies of cortical folding and localization of functional and anatomical boundaries are emerging in both macaque and human brains, with automated methods for generating the sulcus and gyral principle curves becoming available. Active shape methods have presented significant advances as well for studying anatomical shapes, including the active contour and surface deformation work by Terzopoulos (102–105), Pentland & Sclaroff (106–108), and Cootes & Taylor (109–111).

Because of the sheer complexity of human neuroanatomy, in particular the human brain, the study of brain geometry has emerged as the study of the submanifolds of anatomical significance including its landmarks, curves, surfaces, and subvolumes all taken together forming the complete volume. The complete methodology combines mappings that carry all of the submanifolds of points, curves, surfaces, and subvolumes together. This is precisely why in our own group the fundamental transformation group that we have studied are spaces of diffeomorphisms, as they carry these submanifolds consistently. The transformations are constrained to be 1-1 and onto, and differentiable with differentiable inverse, so that connected sets remain connected, submanifolds such as surfaces are mapped as surfaces, and the global relationships between structures are maintained.

THE METRIC SPACE OF ANATOMICAL IMAGES

Geodesics Connecting Geometric Transformation via Diffeomorphisms

The mappings of the geometric or shape type are exclusively invertible, 1-1, onto continuous mappings with continuous inverses that are differentiable, henceforth

called diffeomorphisms. These transformations form a group, denoted by $\mathcal{G}$ with elements $g \in \mathcal{G}$, and the coordinates that they transform are subsets of X. Generally, the low-dimensional transformations—rotation, scale, and skew—are studied in tandem with the infinite dimensional local diffeomorphic transformations. As originally proposed by Christensen et al. (59), one models the transformations as arising from an evolution in time, or a flow $g(t)$, $t \in [0, 1]$ corresponding to the transport equations from continuum mechanics [see Dupuis (65) and Trouvé (60, 76) for their technical development]. The forward and inverse maps are uniquely defined according to $g^{-1}(g(x, t), t) = x$ for all $t \in [0, 1]$, $x \in X$, implying the equations of flow are linked according to

$$\frac{\partial}{\partial t} g(x, t) = v(g(x, t), t), \quad \frac{\partial}{\partial t} g^{-1}(y, t) = -Dg^{-1}(y, t)v(y, t),$$
$$g(0) = g^{-1}(0) = \mathrm{id}, \tag{1}$$

id the identity map, the Jacobian operator giving the $d \times d$ matrix for $\mathbb{R}^d$-valued functions $(Df)_{ij} = \frac{\partial f_i}{\partial x_j}$ and the $d \times 1$ row vector $Df = (\frac{\partial f}{\partial x_1}, \ldots, \frac{\partial f}{\partial x_d})$ for scalar valued functions defined on d–dimensional domain. The flow equations are depicted in panel 1 of Figure 1.

Definition 3.1 *Define the group of transformations $\mathcal{G}$ to be diffeomorphisms $g(1) \in \mathcal{G}$: $x \mapsto g(x, 1) \in X$, 1-1, onto, with continuous inverse and differentiable solutions of Equation 1, with $v(t)$, $t \in [0, 1]$ sufficiently smooth and vanishing at the boundary of X for each t to generate smooth solutions $g(1), g^{-1}(1)$ (60, 65, 76).*

One principal aspect of CA is to define the metric distance between anatomies through the mappings between them. We follow the approach taken in References (60, 68, 71, 76); embed the diffeomorphisms in a Riemannian space and define distance between them via the geodesic length of the flows $g(\cdot)$: $[0, 1] \rightarrow \mathcal{G}$

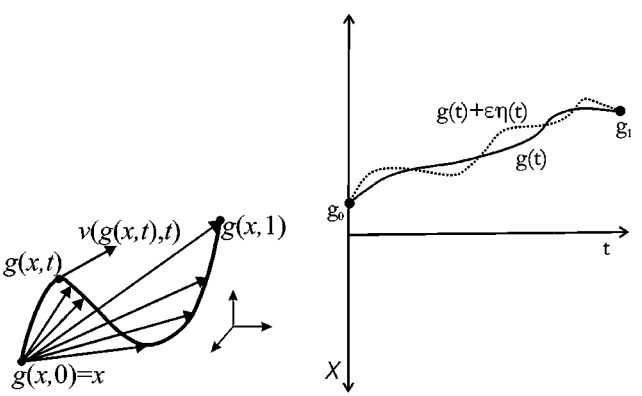

Figure 1 Panel 1 (*left*) shows the Lagrangian description of the flow; panel 2 (*right*) shows the variation of the group flow element $g(\cdot)$ by $\eta(\cdot)$.

which connects them. The geodesic length is defined through the square root of the energy of transformation of the path, $E(g) = \int_0^1 \|v(t)\|_L^2 dt$, $v(t) = \partial g/\partial t$ with $\|\cdot\|_L$ a proper norm on the vector fields on X (i.e., a Sobolev space with L a differential operator). Investigators have used linear differential operators L operating on the vector fields to enforce smoothness on the maps and to define the finite norm, generally differentiating only in space and constructed from the Laplacian and its powers. L is a $d \times d$ matrix of differential operators $L = (L_{ij})$ on $\mathbb{R}^d$ valued vector fields of the form $(Lv)_j = \sum_{i=1}^d L_{ij} v_i$, $j = 1, \ldots, d$ inducing a finite norm constraint at each time t. Denote the norm-squared energy density according to

$$E_v(t) = \int_X E_v(x,t)\,dx = \|v(t)\|_L^2 = \langle Lv(\cdot,t), Lv(\cdot,t)\rangle < \infty, t \in [0,1], \quad (2)$$

so that the solutions of Equation 1 are well defined. The energy density has been defined through powers of the Laplacian for the classic thin-plate splines (16, 29, 30) and the Cauchy-Navier operator for 3-dimensional elasticity (25, 56, 59, 97). Differential operators with sufficient derivatives and proper boundary conditions insure the existence of solutions of the transport equation in the space of diffeomorphic flows (60, 65, 76).

Now the metric between transformations $g_0, g_1 \in \mathcal{G}$ is defined via the length of the shortest path $g(t)$, $t \in [0,1]$ with the boundary conditions $g(0) = g_0$, $g(1) = g_1$. A crucial property of the metric $\rho_{\mathcal{G}}: \mathcal{G} \times \mathcal{G} \to \mathbb{R}^+$ is that it is invariant to $\mathcal{G}$, so that $\rho_{\mathcal{G}}(g_0, g_1) = \rho_{\mathcal{G}}(g \cdot g_0, g \cdot g_1)$ for $g \in \mathcal{G}$, where $g' \cdot g = g \circ g'$.

Theorem 3.1 *The function $\rho_{\mathcal{G}}(\cdot,\cdot)$: $\mathcal{G} \times \mathcal{G} \to \mathbb{R}^+$ between elements $g_0, g_1 \in \mathcal{G}$ defined as*

$$\rho_{\mathcal{G}}(g_0, g_1)^2 = \inf_{g(\cdot): \frac{\partial}{\partial t} g^{-1}(t) = -Dg^{-1}(t)v(t), g(0)=g_0, g(1)=g_1} \int_0^1 E_v(t)\,dt, \quad (3)$$

is a left-invariant metric distance on $\mathcal{G}$. The geodesics satisfy the Euler-Lagrange equations (*proof in Appendix*):

$$\frac{\partial}{\partial t}\nabla_v E_v(\cdot,t) + (Dv(\cdot,t))^t \nabla_v E_v(\cdot,t) + (D\nabla_v E_v(\cdot,t))v(\cdot,t) + \operatorname{div} v(\cdot,t)\nabla_v E_v(\cdot,t) = 0, \quad (4)$$

where ∇ is the gradient operator delivering a vector, $\nabla_v E_v(t) = 2L^\dagger L v(t)$ with the adjoint defined as $\langle Lf, g\rangle = \langle f, L^\dagger g\rangle$, $\operatorname{div} v = \Sigma_i \frac{\partial v}{\partial x_i}$ *the divergence operator.*

Equation 4 was first derived by Mumford (112) who also showed that it reduces to Burger's equation in one-dimension for $L = \mathrm{id}$, $\nabla_v E_v = 2v$. Mumford used a variational argument for calculating Equation 4 perturbing the geodesic by $\eta(t)$, $t \in [0,1]$ leaving the endpoints unchanged (see panel 2 of Figure 1 and appendix). Equation 4 generalizes Arnold's derivation for incompressible flow [Equation 1 of (4)]. The left-invariance follows from that fact that translation by another group element

leaves the distance unchanged because $g(\cdot)$ satisfies $\frac{\partial g(\cdot,t)}{\partial t} = v(g(\cdot,t),t)$, $g(0) = \mathrm{id}$, $g(1) = g_1$ implying $g(0) \circ h = h$, $g(1) = g_1 \circ h$, with an identical velocity field so that $\frac{\partial g(h(x),t)}{\partial t} = v(g(h(x),t),t)$, $g(0) = h$, $g(1) = g_1(h)$. The distances $\rho_{\mathcal{G}}(\mathrm{id}, g) = \rho_{\mathcal{G}}(h, g \circ h)$ are equal for all $h \in \mathcal{G}$. As pointed out by Ratnanather and Baigent (personal communication), the left-invariance of the metric allows the Euler-Lagrange equations to be recast in the Euler-Poincaré form using Marsden's reduction theory (114).

Inducing the Metric Space on Anatomical Images

The group of geometric transformations are not directly observable. Rather images are observed via sensors which measure physical properties of the tissues. Carrying out Grenander's metric pattern theory program, the space or orbit of anatomical images $I \in \mathcal{I}$ must be made into a metric space. The metric distance between anatomical imagery $I \in \mathcal{I}$ is constructed from distances between the mappings $g \in \mathcal{G}$. First, the anatomical orbit of all images is defined.

Definition 3.2 *The mathematical anatomy are functions $I \in \mathcal{I}$, $I : x \in X \mapsto I(x)$, an orbit under the geometric transformations: $\mathcal{I} = \{I' : I'(\cdot) = I(g(\cdot)),\ I \in \mathcal{I}, g \in \mathcal{G}\}$.*

This is a group action (113) on I with $g \cdot I = I \circ g$ and group product $g' \cdot g(\cdot) = g \circ g'(\cdot) = g(g'(\cdot))$, which defines the equivalence relation $I_1 \sim I_2$ if $\exists g \in \mathcal{G}$ such that $I_1(\cdot) = I_2(g(\cdot))$, dividing $\mathcal{I}$ into disjoint orbits.

Now, there can be many high dimensional maps connecting I, I'. For the induced function ρ on $\mathcal{I}$ to be a metric it is required that ρ is invariant to this nonidentifiability; this it inherits from the left-invariance property of $\rho_{\mathcal{G}}$.

Theorem 3.2 *The function $\rho(\cdot,\cdot)$: $\mathcal{I} \times \mathcal{I} \to \mathbb{R}^+$ between elements $I, I' \in \mathcal{I}$ defined as*

$$\rho(I, I')^2 = \inf_{g:\frac{\partial}{\partial t} g^{-1}(t) = -Dg^{-1}(t)v(t),\, I(g^{-1}(\cdot,1)) = I'(\cdot),\, g^{-1}(0) = \mathrm{id}} \int_0^1 E_v(t)\, dt \tag{5}$$

is a metric distance on $\mathcal{I}$ satisfying symmetry and the triangle inequality.

The metric property was proved in References (60, 71, 76). The property sufficient for ρ to be a metric is the left-invariance of ρ [in fact, all that is required is it be invariant to the stabilizer; see (71)]. The fact that $\rho_{\mathcal{G}}$ is left-invariant to $\mathcal{G}$ implies that for all $g \in \mathcal{G}$, $\rho(I \circ g, I' \circ g) = \rho(I, I')$. This also implies any element in the orbit can be taken as the template; all elements are equally good.

Expanding the Metric Space to Incorporate Photometric Variation

Thus far, the metric depends only on the geometric transformations of the background space X. Extend the construction of the metric to be image dependent following Reference (71) by defining the group action to operate on the geometry and photometric values allowing for the creation of new matter. For this, we introduce

an explicit dependence on time in the evolution of the image to accomodate photometric variation via material transport.

Theorem 3.3 *Defining the image evolution in the orbit as* $J(y,t) = I(g^{-1}(y,t),t)$, $\frac{\partial}{\partial t}g^{-1}(y,t) = -Dg^{-1}(y,t)v(y,t)$, *then the function* $\rho(\cdot,\cdot)$: $\mathcal{I}\times\mathcal{I}\to\mathbb{R}^+$ *between elements* $I, I'\in\mathcal{I}$ *defined as*

$$\rho(I,I')^2 = \inf_{v(\cdot),I(\cdot):J(0)=I,J(1)=I'} \int_0^1 \left(\|v(t)\|_L^2 + \left\| \frac{\partial}{\partial t}J(t) + \nabla J^t(t)v(t) \right\|^2 \right) dt \quad (6)$$

is a metric [*proven in* (71)] *satisfying symmetry and the triangle inequality. Defining*

$$\nabla_v E(y,t) = 2L^\dagger L\, v(y,t) + 2\left(\frac{\partial}{\partial t}J(y,t) + \nabla J^t(y,t)v(y,t) \right) \nabla J(y,t), \quad (7)$$

then the Euler Equation 4 holds with boundary term $\nabla_v E\ (\cdot,1) = 0$ *with the geodesics for photometric evolution satisfying* (*proof in Appendix*):

$$L^\dagger L\, v(y,t) + \left(\frac{\partial}{\partial t}J(\cdot,t) + \nabla J^t(\cdot,t)v(\cdot,t) \right) \nabla J(\cdot,t) = 0\,, \quad (8)$$

$$\frac{\partial}{\partial t}\left(\frac{\partial J(\cdot,t)}{\partial t} + \nabla J^t(\cdot,t)v(\cdot,t) \right) + \operatorname{div}\left(\frac{\partial J(\cdot,t)}{\partial t}v(\cdot,t) + (\nabla J^t(\cdot,t)v(\cdot,t))v(\cdot,t) \right) = 0. \quad (9)$$

EULER-LAGRANGE EQUATIONS FOR INEXACT IMAGE MATCHING AND GROWTH

A central problem in CA is essentially diffeomorphic image interpolation, i.e., to infer the geometric image evolution that connects two elements I_0, $I_1\in\mathcal{I}$ under pure geometric evolution. For this a function of the path is defined; call it $I_0(g^{-1}(t))$, $t\in[0,1]$. The goal is to construct the shortest length curve $g(t)$, $t\in[0,1]$ which minimizes the target norm squared $\|I_0(g^{-1}(1)) - I_1\|^2$, as studied in Dupuis et al. (65). This is of course inexact matching, since there is a balance between metric length of the path and target correspondence. We can view the image evolution defined by the geodesic as an interpolation between images via the geodesic. Because of the introduction of the free boundary, there is a boundary term which is introduced.

Theorem 4.1 (Inexact Image Matching) *The minimizer*

$$\inf_{g(\cdot):\frac{\partial}{\partial t}g^{-1}(t) = -Dg^{-1}(t)v(t),g(0)=g_0} \int_0^1 E_v(t)dt + \|I_1 - I_0(g^{-1}(1))\|^2 \quad (10)$$

satisfies the Euler-Lagrange Equation 4 with boundary term (*proof in Appendix*):

$$\nabla_v E_v(\cdot,1) + 2(I_1(\cdot) - I_0(g^{-1}(\cdot,1)))D(I_0(g^{-1}(\cdot,1)))^t = 0, \tag{11}$$

where $D(I_0\,(g^{-1}(\cdot,t))) = \nabla I_0^t(g^{-1}(\cdot,t))\,Dg^{-1}(\cdot,t)$.

The above has no real-time variable, only connection or interpolation between two images via the geodesic. Now assume that the observables define a running norm squared, $\|I_1(t) - I_0(g^{-1}(t))\|^2$, $t \in [0,1]$, corresponding to a time sequence that might occur during space-time growth modelling. Then the problem is akin to finding the trajectory of diffeomorphisms creating observable time flow.

Theorem 4.2 (Space-Time Growth) *The minimizer*

$$\inf_{g:\frac{\partial}{\partial t}g^{-1}(t) = -Dg^{-1}(t)v(t), g(0)=\mathrm{id}, t\in[0,1]} \int_0^1 E_v(t)dt + \int_0^1 \|I_1(t) - I_0(g^{-1}(t))\|^2\,dt \tag{12}$$

satisfies the Euler-Lagrange equation (*proof in Appendix*):

$$\begin{aligned}\frac{\partial}{\partial t}\nabla_v E_v(\cdot,t) + (Dv(\cdot,t))^t\nabla_v E_v(\cdot,t) + (D\nabla_v E_v(\cdot,t))v(\cdot,t)\\ + \operatorname{div} v(\cdot,t)\nabla_v E_v(\cdot,t) = 2(I_1(\cdot,t) - I_0(g^{-1}(\cdot,t)))D(I_0(g^{-1}(\cdot,t)))^t.\end{aligned} \tag{13}$$

COMPUTATIONAL IMAGE MATCHING

Beg's Geometric Transformations via Inexact Matching

In this section, we examine the results of solving the Euler-Lagrange equations for generating the geodesics. Faisal Beg solves inexact image matching (Equation 10) via variations with respect to the velocity field exploiting the vector space structure.

Algorithm 5.1 *Fixed points of the following algorithm* (*proof in supplemental material link in the online version of this chapter or at http://www.annualreviews.org*) *satisfy Equations 4 and 11. Initialize* $v^{old} = 0$, *choose constant* ϵ, *then for all* $t \in [0,1]$,

$$\begin{aligned}&\text{Step 1: } \frac{\partial}{\partial t}g^{new}(t) = v^{old}(g^{new}(t),t),\ \frac{\partial}{\partial t}g^{-1new}(t) = -Dg^{-1new}(t)v^{old}(t),\\ &\qquad \chi^{new}(t) = g^{new}(g^{-1new}(t),1),\\ &\text{Step 2: Compute } v^{new}(t) = v^{old}(t) - \epsilon\nabla_v E(t), \text{ set } v^{old} \leftarrow v^{new}, \text{ return to Step 1}\end{aligned} \tag{14}$$

where

$$\begin{aligned}\nabla_v E(t) = v^{old}(t) + (L^\dagger L)^{-1}\big(|D\chi^{new}(t)|\\ \times D(I_0(g^{-1new}(t)))^t(I_1(\chi^{new}(t)) - I_0(g^{-1new}(t)))\big).\end{aligned} \tag{15}$$

Here $(L^\dagger L)^{-1} f = Kf$ *where* K *is the Green's kernel. The space-time solution of Equation 13 has gradient*

$$\nabla_v E(t) = v^{old}(t) + (L^\dagger L)^{-1}\Bigg(\int_t^1 |D\chi^{new}(t;\tau)| D(I_0(g^{-1new}(t)))^t \times (I_1(\chi^{new}(t;\tau),\tau) - I_0(g^{-1new}(t)))\, d\tau \Bigg) \tag{16}$$

where $\chi(t;\tau) = g(g^{-1}(t),\tau)$

(for proof see supplemental material link in the online version of this chapter or at http://www.annualreviews.org). Notice the smoothing nature of the space-time solution.

Beg's gradient descent algorithm discretizes Equation 15. At the fixed point, the discrete version of the Euler-Lagrange equation is satisfied. Except where noted, the operator is chosen to be $L = -50\nabla^2 + 0.1$ id and the flow time $t \in [0, 1]$ was discretized into 20 timesteps. All geodesic solutions correspond to 10,000 iterations of the gradient algorithm. Results of the mapping of multiple shapes including the forward and inverse diffeomorphic matches for large deformation are shown in Figure 2. Figure 3 shows the results of maps on the geodesic of the flows for the $\frac{1}{2}C$ shape to the C shape (with 30 timesteps) and Heart1 to Heart2 experiments. Figure 4 shows results from the Macaque brain and hippocampus section mapping experiments.

The Psychophysics of the Metric

Shown in Figure 5 are examples of metric computations in 2-D on high resolution electron-micrographs. The mitochondria are shown in increasing order of their metric distance. Here, L is $-50\,\nabla^2 + \text{id}$. Notice how increasing the distance in the metric corresponds closely to one's intuitive feel of closeness and similarity.

Space-Time Flows

The UCLA group of Thompson & Toga (97) has examined the instantaneous version of the growth problem in which, at each time instant, the deformation field is estimated independent of previous time. Figure 6 shows maps of growth in the brains of children, showing growth rates corresponding to the corpus callosum. The maps are made based on scanning the same child at age 7 and 11, and another child at age 8 and 12. Pairs of 3-D scans acquired several years apart are first rigidly registered. A 3-D deformation vector field based on $L = -\nabla^2 + c\nabla\nabla^t$ is constructed at each time point with two components of the deformation field applied to the regular grid overlaid on the anatomy. The Jacobian determinant, whose values are color coded on the deformations shows the local growth rate (red colors, rapid growth).

Photometric Matching with Tumors

We examine photometric variation with $L = \nabla^2 = \frac{\partial^2}{\partial x_1^2} + \frac{\partial^2}{\partial x_2^2}$ and $\|v(t)\|_L^2 = \frac{1}{\alpha} \sum_{i=1}^2 \|\nabla^2 v_i(t)\|^2$ from Equation 6, where α is a positive parameter. Comparison

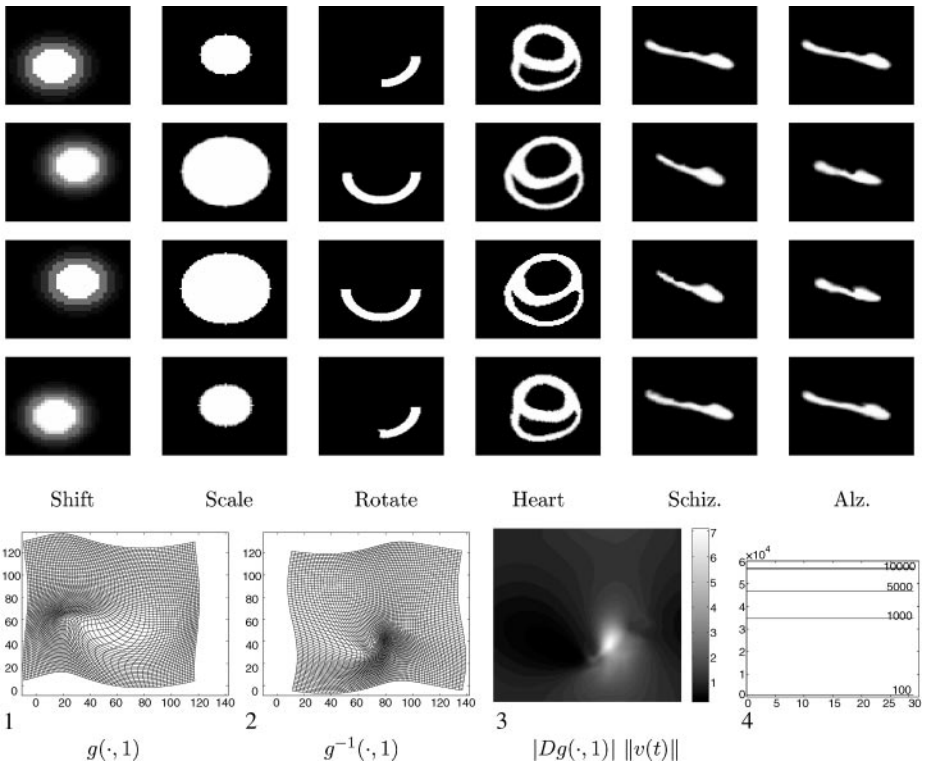

Figure 2 Row 1 shows I_0 and row 2 shows $I_0\,(g^{-1}(\cdot, 1))$; row 3 shows I_1, and row 4 shows I_1 $(g(\cdot, 1))$. Column 1 shows a diagonal shift, column 2 shows a dilation and contraction (scale), column 3 shows a rotational motion (the $\frac{1}{2}C$ shape experiment), column 4 shows a section of Heart 1 matched to corresponding section of Heart 2, and columns 5 and 6 show sections of hippocampus in a young control to that with schizophrenia and with Alzheimer's. Shown in the bottom row are the properties of $g^{-1}_{\frac{1}{2}C}(\cdot, 1)$ (panel 1), the deformation of the underlying coordinate space of the template, $g_{\frac{1}{2}C}(\cdot, 1)$ (panel 2), the deformation of the underlying coordinate space of the target, the Jacobian of the forward map $g(\cdot, 1)$ (panel 3), and the norm of the velocity field along the flow for 1, 100, 1,000, 5,000, 10,000 iterations of the algorithm (panel 4). Notice the geodesic property at the convergence point corresponding to the constant norm $\|v(t)\| = constant$.

between two images I and I' is performed by minimizing over all paths satisfying $v(x, t) = 0$, $t \in [0, 1]$, $x \in \partial X$, and $J(0) = I, J(1) = I'$ as in Reference (71); see algorithm in Supplemental Material link in the online version of this chapter or at http://www.annualreviews.org. Figure 7 shows results demonstrating the transformation process $I(g^{-1}(\cdot, t), t)$ as functions of time $t \in [0, 1]$ between two images I and I'. The top two rows show the process of either creating photometric or geometric change. Depending on the choice of the parameter α, the process

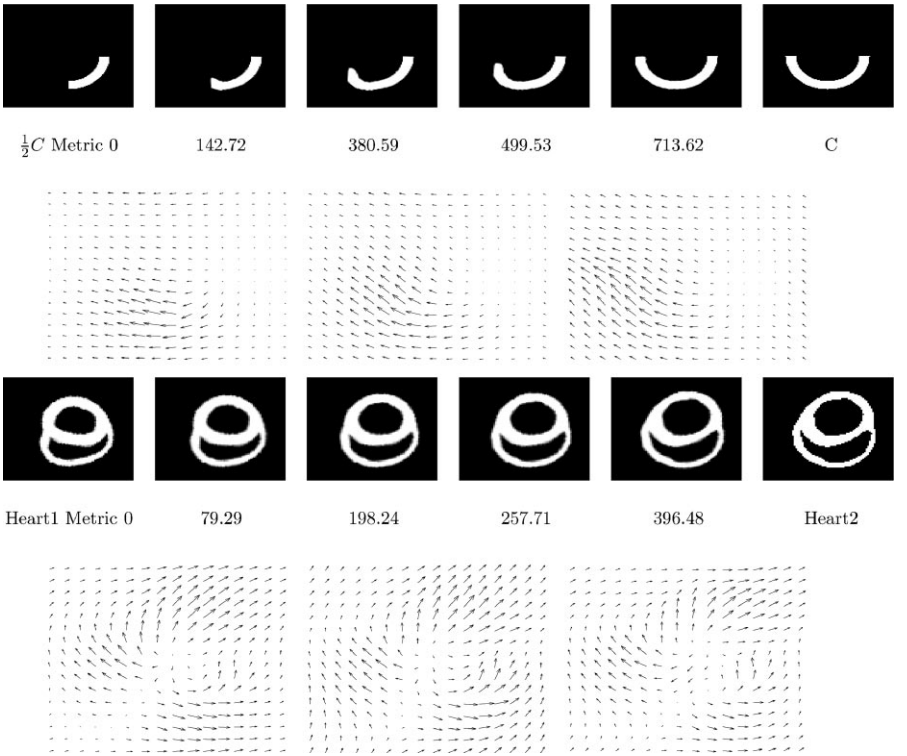

Figure 3 Rows 1 and 3 show images along the geodesic at time points 0 (panel 1), t_3 (panel 2), t_9 (panel 3), t_{12} (panel 4), t_{15} (panel 5), and t_{18} (panel 6). The metric distance from the start point is shown below each panel. Rows 2 and 4 show the vector fields at three different time points on the geodesic, $v(\cdot, t_0)$, $v(\cdot, t_{10})$, $v(\cdot, t_{19})$. The heart data (rows 3, 4) were taken from the laboratory of Dr. Raimond Winslow.

allows for the creation of pixel luminance yielding a transformation that looks like fading with almost no geometric deformation at all (α small), or the process will introduce a large deformation of the grid resembling an explosion (α large). The bottom row of Figure 7 is the result of matching sections of a brain with a tumor shape. The rightmost panel shows the centered black spot.

FINITE DIMENSIONAL SHAPE SPACES

A special class of images corresponding to finite dimensional landmark shapes has been extensively studied by Bookstein (16, 29, 30) and Kendall (115) and colleagues. Fix an integer number of landmarks $N > 0$ and denote by $\mathcal{I}_N = (R^d)^N$ the space of landmarks parameterizing the finite N-shapes through the points that identify them $I_N = (x_1, \ldots, x_N)$, $I'_N = (x'_1, \ldots, x'_N)$. The natural distances between shapes $\rho: \mathcal{I}_N \times \mathcal{I}_N \to \mathbb{R}^+$ are the lengths the paths through which the points must

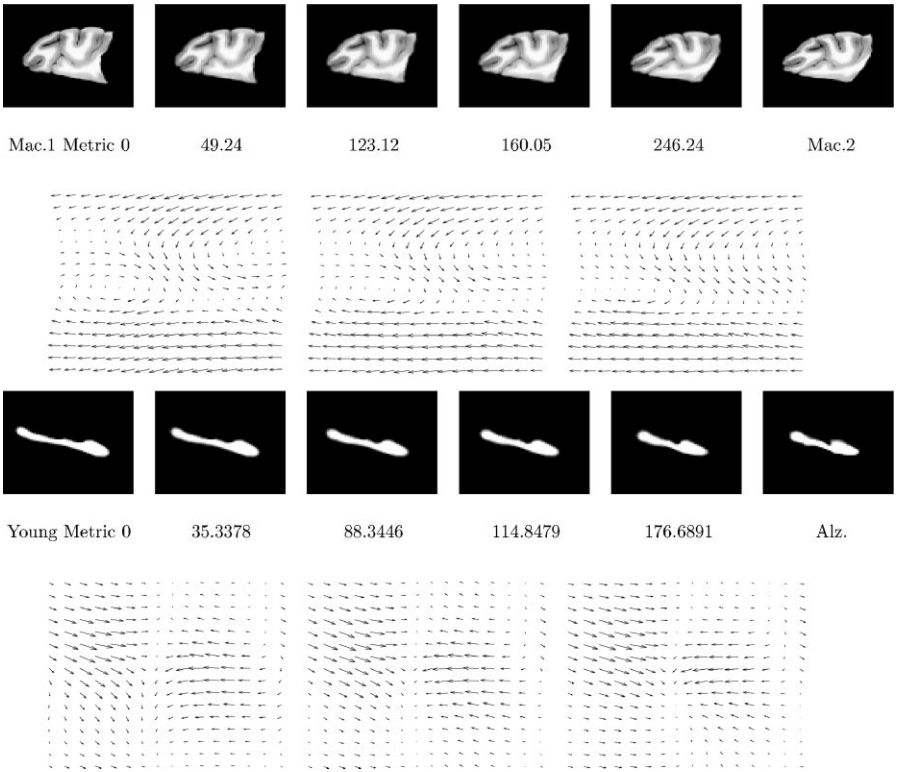

Figure 4 Row 1 shows the maps along the geodesic connecting Macaque1 to Macaque2; row 2 shows the velocity fields along the geodesic for the 2-D matching experiments. The data were taken from the laboratory of Dr. David Van Essen. Rows 3 and 4 show similar results for the hippocampus mappings along the geodesic connecting the young control to the patient with Alzheimer's disease. Row 4 shows velocity fields along the geodesic for the 2-D matching experiments. The data were taken form the laboratory of Dr. John Csernansky.

travel to correspond. Distance is measured through a quadratic form determining the length of the tangent elements as the particles flow.

Definition 6.1 *For N-shapes I_N, I'_N with trajectories $g(t) = (g(x_1, t), \ldots, g(x_N, t))$, in $\mathbb{R}^d$, $g(x_i, 0) = x_i$, $g(x_i, 1) = x'_i$ of length $\int_0^1 \|\frac{\partial g(t)}{\partial t}\|^2_{Q(g(t))}\, dt$, then the geodesic distance is*

$$\rho(I_N, I'_N)^2 = \inf_{g(\cdot): g(x_n,0)=x_n, g(x_n,1)=x'_n} \int_0^1 \sum_{ij=1}^{N} v(g(x_i, t), t)^t\, Q(g(t))_{ij}\, v(g(x_j, t), t)\, dt, \tag{17}$$

where $Q(g(t))$ is an $Nd \times Nd$ positive definite matrix with $d \times d$ blocks $Q(g(t))_{ij}$ with $Nd \times Nd$ inverse $K(g(t)) = (Q(g(t)))^{-1}$, with $d \times d$ blocks $(K(g(t)))_{ij}$.

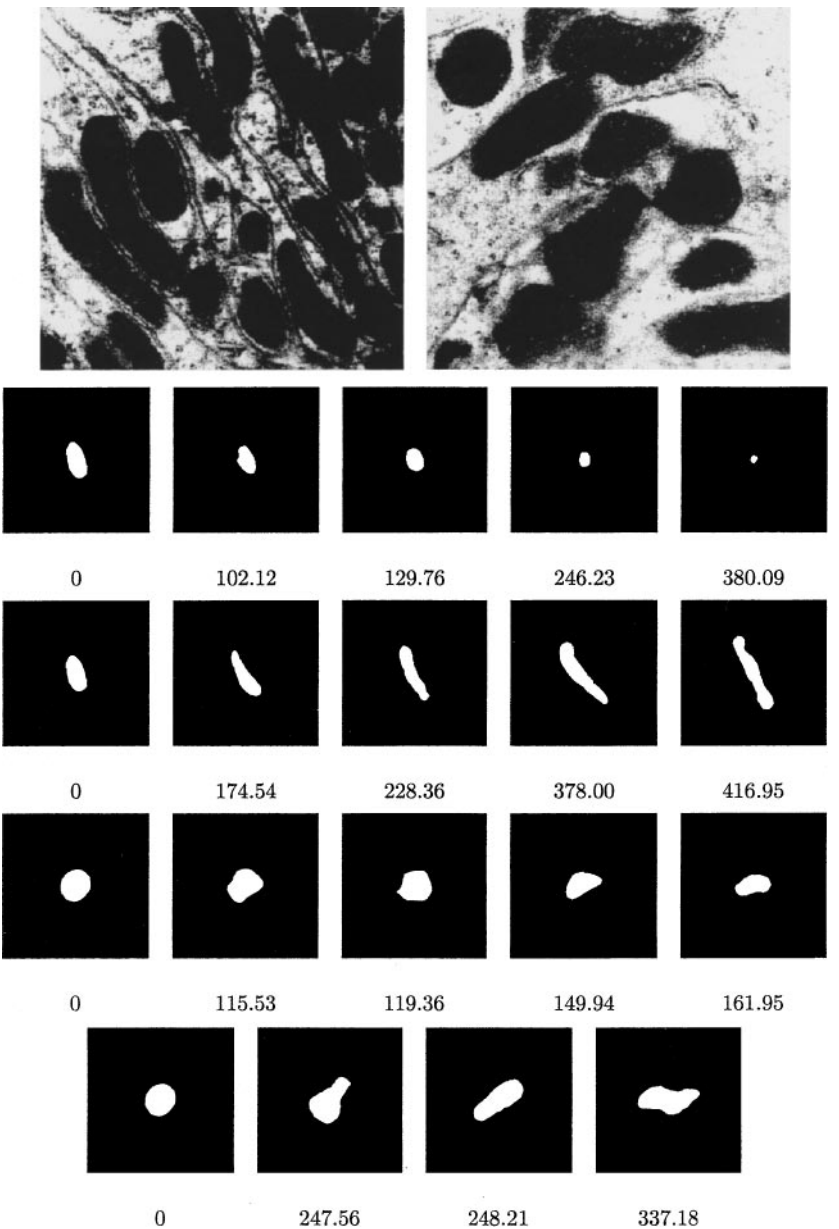

Figure 5 The top row shows the mitochondria subshapes for matching from the laboratory of Dr. Jeffrey Saffitz. Rows 2, 3, 4, and 5 give below each panel the metric for the geodesic distances to indicate which shapes are close and far. Notice how increasing the distance in the metric corresponds to closeness and similarity.

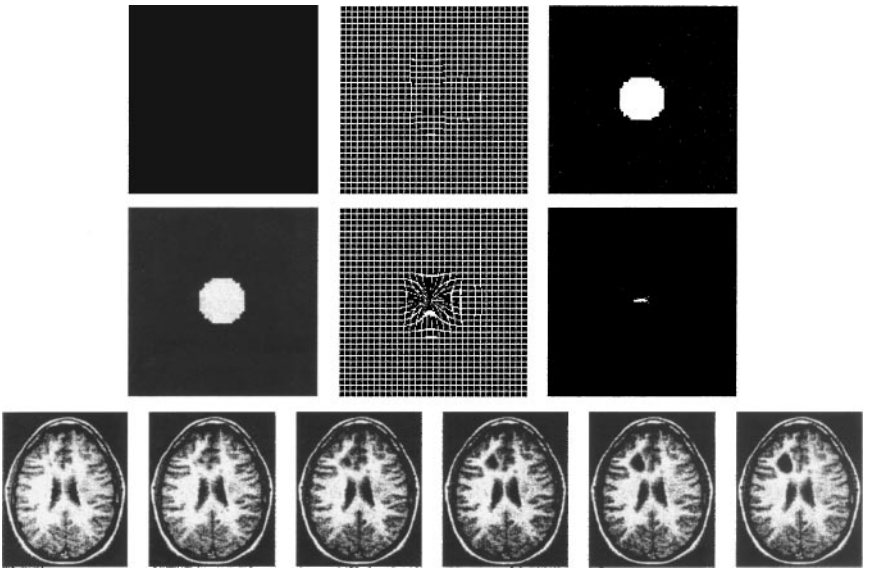

Figure 7 The first row corresponds to small α; the second row corresponds to large α. The left column shows start and end images I_0, I_1; the middle column shows the geometric deformations on the grid determined by mapping $g^{-1}(x, 1)$; the right column shows the image value change. The last row shows a time series of geometric and photometric transformations in generation of tumor in brain tissue. Results from Miller & Younes (71).

Diffeomorphic Landmark Matching in Euclidean Space and the Sphere

MATCHING ON THE CUBE $[0, 1]^d$ The Joshi metric for diffeomorphic matching of landmarks turns out to reduce to the dense matching diffeomorphism only involving the paths of the landmarks. These are the Joshi diffeomorphism splines as first shown in (69). Assume the the quadratic form $\|v(t)\|_L^2$ admits $d \times d$ Green's kernel K so that for all f in the space $\| f \|_L$ finite,

$$\langle K(x, \cdot),\ f \rangle_L = \int_X L^\dagger L K(x, y) f(y)\, dy = f(x). \tag{18}$$

Theorem 6.1 (Joshi (69)) *For N-shapes* I_N, $I'_N \in \mathbb{R}^{dN}$, $\frac{\partial}{\partial t} g(x, t) = v(g(x, t), t)$, $g(x_n, 0) = x_n$, $g(x_n, 1) = x'_n$ *the optimizing diffeomorphism satisfying*

$$\inf_{v: R_0^1 \|v(\cdot,t)\|^2 dt < \infty} \int_0^1 \|v(\cdot, t)\|_L^2 dt + \sum_{n=1}^N \frac{\|y_n - g(x_n, 1)\|_{\mathbb{R}^d}^2}{\sigma^2}, \tag{19}$$

with $Nd \times Nd$ Green's kernel $K(g(t))$, inverse $Q(g(t)) = K^{-1}(g(t))$ where

$$K(g(t)) = \begin{pmatrix} K(g(x_1,t), g(x_1,t)) & \cdots & K(g(x_1,t), g(x_N,t)) \\ \vdots & \vdots & \vdots \\ K(g(x_N,t), g(x_1,t)) & \cdots & K(g(x_N,t), g(x_N,t)) \end{pmatrix}$$

is given by

$$v(\cdot,t) = \sum_{i=1}^{N} K(g(x_i,t),\cdot) \sum_{n=1}^{N} Q(g(t))_{in}\, \dot{g}(x_n,t)$$

and

$$g(x_n,\cdot)n = 1,\ldots,N = \underset{\dot{g}(x_n,\cdot)n=1,\ldots,N}{\operatorname{argmin}} \int_0^1 \sum_{ij} \dot{g}(x_i,t)^t\, Q(g(t))_{ij}\, \dot{g}(x_j,t)\, dt + \sum_{n=1}^{N} \frac{\|y_n - g(x_n,1)\|^2_{\mathbb{R}^d}}{\sigma^2}$$

(*proof in supplemental material link in the online version of this chapter or at http://www.annualreviews.org*).

Joshi (69) examines the matching problem in Euclidean subsets of $\mathbb{R}^n$ following the gradient of the cost in the plane $n=2$, and cubic volumes $n=3$ choosing operators constructed from the Laplacian $L = \operatorname{diag}(-\nabla^2 + cI)$, studying both exact and inexact landmark matching. In $\mathbb{R}^3$, the 3×3 diagonal blocks $K(x, y) = \operatorname{diag}[\kappa e^{-\sqrt{\frac{1}{c}}\|y-x\|}]$ with κ normalizing $\kappa \int e^{-\sqrt{\frac{1}{c}}\|y-x\|}\, dy = 1$. The top row of Figure 8 shows the matching for the "OVAL" and "S" (*panels 1 and 2*) from Joshi's gradient algorithm (69). The corresponding points were used as landmarks with variances $\sigma^2 = 0.1$ (*panel 3*) and $\sigma^2 = 10$ (*panel 4*).

Matching on the Sphere S^2: Investigators in CA, beginning with the earliest work of Dale & Sereno (34), have introduced transformations on the sphere to study the neocortex. Bakircioglu et al. (70) constructed diffeomorphisms on the sphere via maps that are constrained to satisfy flow equations $\frac{\partial}{\partial t} g(x,t) = v(g(x,t),t)$, $g(x,0) = x$, $t \in [0,1]$, $x \in S^2$, $v(x,t) = \sum_{i=1}^{2} v_i(x,t)\, E_i(x)$; where $E_1(\cdot)$, $E_2(\cdot)$ are coordinate frames on the sphere from stereographic projection.

For smoothing, the spherical Laplacian operator is used ($L = \frac{\partial^2}{\partial\phi^2} + \cot\phi \frac{\partial}{\partial\phi} + \frac{1}{\sin^2\phi}\frac{\partial^2}{\partial\theta^2}$), which has as eigenfunctions the spherical harmonics (116) inducing the $2N \times 2N$ diagonal block matrix

$$K(g(t))_{ij} = \operatorname{diag}\left[\sum_{n=1}^{\infty} \frac{1}{n^2(n+1)^2} \frac{2n+1}{4\pi} P_n(\cos(\Psi(g(x_i,t), g(x_j,t)))) \right],$$

with the spherical solid angle $\Psi(\cdot,\cdot)$ and Legendre polynomials $P_n(x) = \frac{1}{2^n n!}\frac{d^n}{dx^n}(x^2-1)^n$.

Given N-landmarks x_n, y_n, $n=1, \ldots, N \subset S^2$, with distance on the sphere Ψ and coordinate frames on the sphere E_1, E_2, the optimal diffeomorphism satisfying $\frac{\partial}{\partial t} g(\cdot, t) = \sum_{i=1}^2 v_i(g(\cdot, t), t) E_i(g(\cdot, t))$, $g(x, 0) = x$, $x \in S^2$, minimizing $\sum_{i=1}^2 \int_{S^2 \times [0,1]} \nabla^2 |v_i(x(\theta, \psi), t)|^2 \sin \psi d\psi d\theta$ is given by

$$\inf_{g:\dot{g}(t)=\mathrm{P}_{i=1}^2 v_i(g(t),t)E_i(g(t))} \int_0^1 \sum_{ij} v(x_i, t)^t (K(g(t))^{-1})_{ij} v(x_j, t)\, dt + \sum_{n=1}^N \frac{\Psi^2(y_n, g(x_n, 1))}{\sigma_n^2}.$$

The results of computations of spherical deformations are shown in the bottom row of Figure 8.

Mapping the Cerebral Cortex

To understand individual variations in the cortical topography, the Van Essen group has been using large deformations to establish correspondences between the cortical maps of various individual cortical surfaces (66, 100, 101). The left column of Figure 9 shows a surface-based atlas of the macaque visual cortex. The top panel shows the macaque surface in 3-D and the bottom panel shows the flat atlas. The right column of Figure 9 shows results from flat mapping transformations of the macaque. The top row of Figure 10 shows an interspecies comparison via cortical surface deformation between the macaque and visible human (100).

Landmark Matching Via Other Metric Distances

EUCLIDEAN DISTANCE AND BOOKSTEIN THIN-PLATE SPLINE DISTANCE Euclidean distance between N-shapes in $\mathbb{R}^d$ measures distance according to straight line paths between the objects. Choosing the quadratic form to be a constant independent of the path, the metric distance becomes $\rho(I_N, I'_N)^2 = \sum_{ij=1}^N (x_i - x'_i)^t (K^{-1})_{ij} (x_j - x'_j)$.

Bookstein's (16, 29, 30) thin-plate spline landmark matching measure approximates the tangent flow of the landmark trajectories by the tangent at the origin. This is clearly not symmetric, nor does it satisfy the triangle inequality. However, for small deformations, this is a powerful methodology that approximates the diffeomorphic flow metric of Joshi in the tangent space by the metric at the origin. Assume Green's operator as the $dN \times dN$ block matrix $K(g(0))$ evaluated at the origin of the flow with $d \times d$ blocks $K(g(0))_{ij}$. The approximate distance reduces to $\tilde{\rho}(I_N, I'_N)^2 = \sum_{ij=1}^N (x_i - x'_i)^t (K(g(0))^{-1})_{ij} (x_j - x'_j)$.

KENDALL'S SIMILITUDE INVARIANT DISTANCE Kendall (115) defines the distance between sets of N-shapes invariant to uniform scale, rotation, and translation. Define the affine similitudes to be matrices $A = sO$, $s \in (0, \infty)$, $O \in SO(n)$, with their

action on the shapes, the scale-rotation-translation of each point of the shape: $AI + a = (Ax_1 + a, \ldots, Ax_N + a)^t$. The Kendall invariant distance requires the matrices $K(I_N)$ have the property that, for all (A, a), $K(AI_N + a) = AK(I_N)A^t$.

Theorem 6.2 [Kendall (115)] *Defining the mean shape position as* $\bar{g}(t) = \frac{1}{N}\sum_{n=1}^{N} g(x_n, t)$, *with* $K(g(t)) = \sigma^2(g(t))\mathrm{id}$, *where* id *is the* $Nd \times Nd$ *identity matrix and* $\sigma^2(g(t)) = \sum_{i=1}^{N} \|g(x_i, t) - \bar{g}(t)\|^2$, *with* ρ_0 *a distance on* $\mathbb{R}^+ \times \mathbb{R}^d$, *the geodesic connecting* I_N, I'_N *minimizing* $\sum_{i=1}^{N} \int_0^1 \frac{1}{\sigma^2(g(t))} \left\| \frac{\partial g}{\partial t}(x_i, t) \right\|^2 dt$ *has distance* (*proof in Appendix*)

$$\rho(I_N, I'_N)^2 = \rho_0((\sigma(g(0)), \bar{g}(0)), (\sigma(g(1)), \bar{g}(1)))^2 + \left(\arccos \sum_{i=1}^{N} \left\langle \frac{g(x_i, 0) - \bar{g}(0)}{\sigma(g(0))}, \frac{g(x_i, 1) - \bar{g}(1)}{\sigma(g(1))} \right\rangle \right)^2 \quad (20)$$

with Kendall's similitude invariant distance given by

$$\tilde{\rho}(I_N, I'_N) = \inf\{\rho(AI_N + a, I'_N), A \text{ similitude}, a \in \mathbb{R}^d\}. \quad (21)$$

Kendall's distance $\tilde{\rho}$ in Equation 21 requires computing the minimum of $\rho(sOI_N + a, I'_N)$, for $s > 0$, $O \in SO(d)$ and $a \in \mathbb{R}^d$. Defining the normalized landmarks by $\gamma(x_i, t) = \frac{g(x_i,t) - \bar{g}(t)}{\sigma(g(t))}$, then because the action of s and a does not affect $\gamma(x_i, \cdot)$; one can select them in order to cancel the distance ρ_0 without changing the second term, implying that $\tilde{\rho}(I_N, I'_N)$ is the minimum of $\arccos \sum_{i=1}^{N} \langle \gamma_i(x_i, 0), O\gamma_i(x_i, 1) \rangle$ when O varies in $SO(d)$. When $d = 2$, there is an explicit solution $\tilde{\rho}(I_N, I'_N) = \arccos \left| \sum_{i=1}^{N} \langle \gamma_i(0, x_i), \gamma_i(1, x_i) \rangle \right|$.

PROBABILISTIC MEASURES OF VARIATION AND STATISTICAL INFERENCE

For constructing probability measures of anatomical variation the Grenander school characterizes shape as Gaussian fields indexed over the manifolds on which the vector fields are defined (1, 2, 64, 118, 118a). Associate with the diffeomorphic maps $g: I \to I'$ the vector fields modulo the identity map as a 3-dimensional Gaussian vector field $\{U(x), = g(x) - x, x \in M\}$ on the smooth sub-manifold of the full brain volume $M \subset X$. Expand the Gaussian field using a complete orthonormal basis on the background space M; the U-field becomes $U(\cdot) = \sum_k u_k \psi_k(\cdot)$, where u_k are independent Gaussian random variables with fixed means and covariances, and ψ_k a complete orthonormal base. Complete orthonormal bases are constructed via calculation of empirical covariances and their eigenfunctions.

The Csernansky group has been quantifying the variation of the shape of the hippocampus subvolumes in brains via magnetic resonance imagery (61, 62, 119, 120). CA methods have been used to identify deformations in the shape of the hippocampus that strongly discriminate subjects with schizophrenia from matched controls (119) and quantify the mildest forms of Alzheimer's Disease (AD) (120). The

statistical covariation of hippocampus shape from the populations are grouped into n_1 controls and n_2 test cases. The maps are represented via the n-vectors of coefficients $U=(u_1,\ldots,u_n)^t$, where $U(x)=\sum_{k=1}^{n} u_k\psi_k(x)$. Wang et al. (121) have shown that logistic regressions based on χ^2 scoring of the groups of coefficients indicate that 3–5 basis functions are sufficient for describing group differences. The U^1, U^2-vectors are modelled as Gaussian, with empirical means $\hat{U}^1=\frac{1}{n_1}\sum_{i=1}^{n_1} U_i^1$, $\hat{U}^2=\frac{1}{n_2}\sum_{j=1}^{n_2} U_j^2$, and common covariances:

$$\hat{\Sigma}=\frac{1}{n_1+n_2-2}\left(\sum_{i=1}^{n_1}\left(U_i^1-\hat{U}^1\right)\left(U_i^1-\hat{U}^1\right)^t+\sum_{j=1}^{n_2}\left(U_j^2-\hat{U}^2\right)\left(U_j^2-\hat{U}^2\right)^t\right). \tag{22}$$

The hypothesis test of the two group means with unknown but common covariance for the null hypothesis, $\mathcal{H}_0$: $\bar{U}^1=\bar{U}^2$, has the Hotelling's T^2 statistic given by $T^2=\frac{n_1n_2}{n_1+n_2}(\hat{U}^1-\hat{U}^2)^T\hat{\Sigma}^{-1}(\hat{U}^1-\hat{U}^2)$. The sample means $\hat{U}^1$ and $\hat{U}^2$ are therefore normally distributed with means $\bar{U}^1$, $\bar{U}^2$, and common covariance $\frac{1}{n_1}\Sigma$, with $\sqrt{n_1n_2/(n_1+n_2)}(\hat{U}^1-\hat{U}^2)$ normally distributed, covariance Σ under the null hypothesis. Following (122, p. 109), $(n_1+n_2-2)\hat{\Sigma}$ is distributed as $\Sigma_{i=1}^{n_1+n_2-2}X_iX_i^t$ where X_i is distributed according to $\mathcal{N}(0,\Sigma)$. Thus, T^2 has an F distribution, and the null hypothesis $\mathcal{H}_0$ is rejected with a significance level α if

$$T^2\geq\frac{(n_1+n_2-2)K}{n_1+n_2-K-1}F^*_{K,n_1+n_2-K-1}(\alpha), \tag{23}$$

where $F^*_{K,n_1+n_2-K-1}(\alpha)$ denotes the upper $100\alpha\%$ point of the F_{K,n_1+n_2-K-1} distribution, and K is the total number of basis functions used in calculating the T^2 statistics. The log-likelihood ratio for hypothesis testing is

$$\begin{aligned}\Lambda=&-\frac{1}{2}(U_i-\hat{U}^{\text{schiz}})^T\hat{\Sigma}^{-1}(U_i-\hat{U}^{\text{schiz}})\\&+\frac{1}{2}(U_i-\hat{U}^{\text{ctrl}})^T\hat{\Sigma}^{-1}(U_i-\hat{U}^{\text{ctrl}}).\end{aligned} \tag{24}$$

The vector coefficients represent the coefficients for the principal components used in the study. Under H_0, H_1 the log-likelihood ratio Λ ($\Lambda<0$, ≥ 0, respectively) has sufficient statistic Gaussian distributed with means variances $\bar{U}_0$, σ_0^2, $\bar{U}_1$, and variance σ_1^2, respectively.

Wang et al. (121) have found that scale and volume are not powerful discriminants of group difference in the schizophrenic and normal populations; however, shape difference is. Figure 11 examines results from AD, normal aging and schizophrenia. The top row shows the difference of hippocampal surface patterns between the controls and targets groups (left: AD, middle: normal aging, right: schizophrenia) visualized as z-scores on the mean surface.

Joshi showed that Fisher's method of randomization can be used to derive a distribution-free estimate of the level of significance of the difference. For all permutations of the given two groups, the means and covariances are calculated from

Monte Carlo simulations generating 10,000 uniformly distributed random permutations. The collection of T^2 statistics from each permutation gives rise to an empirical distribution $\hat{F}(\cdot)$ estimating $F(\cdot)$ in Equation 23 using $F_{K,n_1+n_2-K-1} = \frac{n_1+n_2-K-1}{(n_1+n_2-2)K} T^2$. The null hypothesis that the two groups have equal means is rejected when $p = \int_{T^2}^{\infty} \hat{F}(f)\,df$ falls below a predefined significance level. The Gaussian assumption for the coefficient vectors are valid since the empirical distribution of the $\hat{F}$ statistics follows the F-distribution curve.

SUMMARY

This paper reviews recent developments in the formulation of metric spaces for studying biological shapes in computational anatomy. We expect that such a formulation will provide the fundamental basis for future developments in the quantification of growth and form.

ACKNOWLEDGMENTS

We would like to acknowledge Richard Rabbitt for introducing the concept of flows. We would like to acknowledge Ulf Grenander and David Mumford for their continued involvement in the mathematical formulation of the emerging discipline of computational anatomy. We would like to acknowledge Drs. John Csernansky and David van Essen of Washington University for their neuro-scientific collaborations in CA. We would like to acknowledge Faisal Beg and Tilak Ratnanather for their involvement in the development of the manuscript. This work was supported by the National Institute of Health grants 5 RO1 MH60974-07, PO1 AG03991-16, 1 RO1 MH60883-01, 1 RO1 MH62626-01, P41 RR15241, and 1 P20 MH6211300A1 and Office of Naval Research grant N00014-00-1-0327.

LITERATURE CITED

1. Miller MI, Banerjee A, Christensen GE, Joshi SC, Khaneja N, et al. 1997. Statistical methods in computational anatomy. *Stat. Methods Med. Res.* 6:267–99
2. Grenander U, Miller MI. 1998. Computational anatomy: an emerging discipline. *Q. App. Math.* 56:617–94
3. Grenander U. 1993. *General Pattern Theory*. Oxford, UK: Oxford Univ. Press. 883 pp.
4. Arnold VI, Khesin BA. 1992. Topological methods in hydrodynamics. *Annu. Rev. Fluid Mech.* 24:145–66
5. Pechura CM, Martin JB, eds. 1991. *Mapping the Brain and Its Functions: Integrating Enabling Technologies in Neuroscience Research.* Washington, DC: Natl. Acad. 180 pp.
6. Greitz T, Bohm C, Holte S, Eriksson L. 1991. A computerized brain atlas: construction, anatomical content, and some applications. *J. Comp. Assist. Tomog.* 15(1):26–38

7. Bajcsy R, Lieberson R, Reivich M. 1983. A computerized system for the elastic matching of deformed radiographic images to idealized atlas images. *J. Comp. Assist. Tomog.* 7:618–25
8. Dann R, Hoford J, Kovacic S, Reivich M, Bajcsy R. 1989. Evaluation of elastic matching systems for anatomic (CT, MR) and functional (PET) cerebral images. *J. Comp. Assist. Tomog.* 13(4):603–11
9. Hohne KH, Bomans M, Reimer M, Schubert R, Tiede U, Lierse W. 1992. A volume-based anatomical atlas. *IEEE Comput. Graph. Appl.* 12:72–78
10. Mazziotta JC, Toga AW, Evans AC, Fox P, Lancaster J. 1995. Probabilistic atlas of the human brain: theory and rationale for its development. *Neuroimage* 2:89–101
11. Thompson PM, Mega MS, Narr KL, Sowell ER, Blanton RE, Toga AW. 2000. Brain image analysis and atlas construction. In *Handbook of Medical Imaging*, Vol. 2. *Medical Image Processing and Analysis*, ed. M Sonka, JM Fitzpatrick, pp. 1061–129. Bellingham, WA: SPIE
12. Mazziotta J, Toga A, Evans A, Fox P, Lancaster J, et al. 2001. A probabilistic atlas and reference system for the human brain: international consortium for brain mapping (ICBM). *Philos. Trans. R. Soc. London B* 356:1293–322
13. Rademacher J, Galaburda AM, Kennedy DN, Filipek PA, Caviness VS Jr. 1992. Human cerebral cortex: localization, parcellation, and morphometry with magnetic resonance imaging. *J. Cogn. Neurosci.* 4(4):352–74
14. Rademacher J, Caviness VS Jr, Steinmetz H, Galaburda AM. 1993. Topographical variation of the human primary cortices. *Cereb. Cortex* 3:313–29
15. Shenton ME, Kikinis R, Jolesz FA, Pollak SD, LeMay M, et al. 1992. Abnormalities of the left temporal lobe and thought disorder in schizophrenia. *N. Engl. J. Med.* 327:604–12
16. Bookstein FL. 1978. *The Measurement of Biological Shape and Shape Change*, Vol. 24. *Lecture Notes in Biomathematics*. New York: Springer-Verlag
17. Feldmar J, Ayache N, Betting F. 1997. 3D-2D projective registration of free-form curves and surfaces. *Comput. Vis. Image Underst.* 65(3):403–24
18. Guimond A, Roche A, Ayache N, Meunier J. 2001. Multimodal brain warping using the Demons algorithm and adaptative intensity corrections. *IEEE Trans. Med. Imaging* 20(1):58–69
19. Cachier P, Mangin J-F, Pennec X, Rivière D, Papadopoulos-Orfanos D, et al. 2001. Multisubject non-rigid registration of brain MRI using intensity and geometric features. In *4th Int. Conf. Med. Image Comput. Comput.-Assist. Intervent.* (*MICCAI'01*), Vol. 2208, *LNCS*, ed. WJ Niessen, MA Viergever, pp. 734–42. Heidelberg: Springer-Verlag
20. Ayache N. 2002. Medical imaging informatics. From digital anatomy to virtual scalpels and image guided therapy. *IMIA Yearbk. Med. Inform*, ed. R Haux, C Kulikowski, pp. 1–2. Stuttgart: Schattaver
21. Thirion JPh, Goudon A. 1995. Computing the differential characteristics of isointensity surfaces. *Comp. Vis. Image Underst.* 61(2):190–202
22. Thirion JPh, Goudon A. 1996. The 3D marching lines algorithm. *Graph. Models Image Process.* 58(6):503–9
23. Bajcsy R, Kovacic S. 1989. Multiresolution elastic matching. *Comput. Vis. Graph. Image Process.* 46:1–21
24. Gee J, Briquer LL, Haynor DR, Bajcsy R. 1994. Matching structural images of the human brain using statistical and geometrical image features. In *SPIE Proc. Visual. Biomed. Comput. 1994*, ed. RA Robb, 2359:191–204. Bellingham, WA: SPIE
25. Gee JC, Bajcsy RK. 1999. Elastic matching: continuum mechanical and probabilistic analysis. See Ref. 123, pp. 183–97

26. Gee JC, Haynor DR. 1999. Numerical methods for high-dimensional warps. See Ref. 123, pp. 101–113
27. Gee JC. 1999. On matching brain volumes. *Pattern Recognit.* 32:99–111
28. Bookstein FL, Green WDK. 1992. Edge information at landmarks in medical images. In *SPIE Proc. Visual. Biomed. Comput. 1992*, ed. RA Robb, 1808:242–58. Bellingham, WA: SPIE
29. Bookstein FL. 1991. *Morphometric Tools for Landmark Data*. New York: Cambridge Univ. Press
30. Bookstein FL. 1996. Biometrics, biomathematics and the morphometric synthesis. *Bull. Math. Biol.* 58:313–65
31. Rangarajan A, Chui H, Bookstein FL. 1997. The softassign procrustes matching algorithm. In *Information Processing in Medical Imaging* (*IPMI'97*), Vol. 1230, *LNCS*, ed. J. Duncan, G Gidi, pp. 29–42. Heidelberg: Springer-Verlag
32. Bookstein FL. 1997. Shape and the information in medical images: a decade of the morphometric synthesis. *Comput. Vis. Image Underst.* 66:97–118
33. Andresen PR, Bookstein FL, Conradsen K, Ersbll BK, Marsh JL, Kreiborg S. 2000. Surface-bounded growth modeling applied to human mandibles. *IEEE Trans. Med. Imaging* 19:1053–63
34. Dale AM, Sereno MI. 1993. Improved localization of cortical activity by combining EEG and MEG with MRI cortical surface reconstruction: a linear approach. *J. Cogn. Neurosci.* 5:162–76
35. Dale AM, Fischl B, Sereno MI. 1999. Cortical surface-based analysis. I. Segmentation and surface reconstruction. *Neuroimage* 9(2):179–94
36. Fischl B, Sereno MI, Dale AM. 1999. Cortical surface-based analysis. II. Inflation, flattening, and a surface-based coordinate system. *Neuroimage* 9(2): 195–207
37. Fischl B, Sereno MI, Tootell RBH, Dale AM. 1999. High-resolution intersubject averaging and a coordinate system for the cortical surface. *Human Brain Mapp.* 8(4):272–84
38. Wang Y, Staib LH. 1998. Integrated approaches to non-rigid registration in medical images. *Proc. IEEE Worksh. Appl. Comput. Vis.*, 4th, pp. 102–8, Princeton, NJ
39. Wang Y, Staib LH. 1998. Elastic model based non-rigid registration incorporating statistical shape information. *Proc. Int. Conf. Med. Image Comput. Comput.-Assist. Inter.*, 1st, pp. 1162–73, Cambridge, MA
40. Staib LH, Duncan JS. 1992. Boundary finding with parametrically deformable models. *IEEE Trans. Pattern Anal. Mach. Intell.* 14:1061–75
41. Chakraborty A, Staib LH, Duncan JS. 1996. Deformable boundary finding in medical images by integrating gradient and region information. *IEEE Trans. Med. Imaging* 15:859–70
42. Chakraborty A, Duncan JS. 1999. Game-theoretic integration for image segmentation. *IEEE Trans. Pattern Anal. Mach. Intell.* 21:12–30
43. Wang Y, Peterson BS, Staib LH. 2000. Shape-based 3D surface correspondence using geodesics and local geometry. *Comput. Vis. Pattern Recognit.* 2:644–51
44. Wang Y, Staib LH. 2000. Boundary finding with prior shape and smoothness models. *IEEE Trans. Pattern Anal. Mach. Intell.* 9(22):738–43
45. Evans AC, Beil C, Marret S, Thompson CJ, Hakim A. 1988. Anatomical-functional correlation using an adjustable MRI-based region of interest atlas with positron emission tomography. *J. Cereb. Blood Flow Metab.* 8:513–30
46. Evans AC, Dai W, Collins L, Neelin P, Marret S. 1991. Warping of a computerized 3-D atlas to match brain image volumes for quantitative neuroanatomical and functional analysis. *Image Process.* 1445:236–46
47. Collins DL, Neelin P, Peters TM, Evans

AC. 1994. Automatic 3D intersubject registration of MR volumetric data in standardized Talairach space. *J. Comp. Assist. Tomog.* 18:192–205
48. Friston KJ, Ashburner J, Frith CD, Poline J-B, Heather JD, et al. 1995. Spatial registration and normalization of images. *Human Brain Mapp.* 2:165–89
49. Collins DL, Holmes CJ, Peters TM, Evans AC. 1995. Automatic 3-D model-based neuroanatomical segmentation. *Humen Brain Mapp.* 3:190–208
50. Evans AC, Collins DL, Holmes CJ. 1996. Computational approaches to quantifying human neuroanatomical variability. In *Brain Mapping: The Methods*, ed. J Mazziotta, AW Toga, pp. 343–61. San Diego: Academic
51. Paus T, Zijdenbos A, Worsley K, Collins DL, Blumenthal J, et al. 1999. Structural maturation of neural pathways in children and adolescents: in vivo study. *Science* 283:1908–11
52. Rapoport JL, Giedd JN, Blumenthal J, Hamburger S, Jeffries N, et al. 1999. Progressive cortical change during adolescence in childhood-onset schizophrenia. A longitudinal magnetic resonance imaging study. *Arch. Gen. Psychiatry* 56:649–54
53. Chung MK, Worsley KJ, Paus T, Cherif C, Collins DL, et al. 2001. A unified statistical approach to deformation-based morphometry. *NeuroImage* 14:595–606
54. Friston KJ, Frith CD, Liddle PF, Frackowiak RSJ. 1991. Plastic transformation of PET images. *J. Comp. Assist. Tomog.* 15:634–39
55. Good CD, Johnsrude IS, Ashburner J, Henson RNA, Friston KJ, Frackowiak RSJ. 2001. A voxel-based morphometric study of ageing in 465 normal adult human brains. *NeuroImage* 14:21–36
56. Miller MI, Christensen GE, Amit Y, Grenander U. 1993. Mathematical textbook of deformable neuroanatomies. *Proc. Nat. Acad. Sci. USA* 90:11944–48
57. Grenander U, Miller MI. 1994. Representations of knowledge in complex systems. *J. R. Stat. Soc. B* 56(3):549–603
58. Joshi SC, Miller MI, Christensen GE, Banerjee A, Coogan TA, Grenander U. 1995. Hierarchical brain mapping via a generalized dirichlet solution for mapping brain manifolds. *Proc. SPIE Int. Symp. Opt. Sci. Eng. Instr.* 2573:278–89
59. Christensen GE, Rabbitt RD, Miller MI. 1996. Deformable templates using large deformation kinematics. *IEEE Trans. Image Process.* 5:1435–47
60. Trouvé A. 1995. Action de groupe de dimension infinie et reconnaissance de formes. *C. R. Acad. Sci. Paris Sér. I* 321: 1031–34
61. Haller JW, Christensen GE, Joshi SC, Newcomer JW, Miller MI, et al. 1996. Hippocampal MR imaging morphometry by means of general pattern matching. *Radiology* 199:787–91
62. Haller JW, Banerjee A, Christensen GE, Joshi SC, Miller MI, et al. 1997. Three-dimensional hippocampal volumetry by high dimensional transformation of a neuroanatomical atlas. *Radiology* 202:504–10
63. Christensen GE, Joshi SC, Miller MI. 1997. Volumetric transformation of brain anatomy. *IEEE Trans. Med. Imaging* 16(6):864–77
64. Joshi SC, Miller MI, Grenander U. 1997. On the geometry and shape of brain submanifolds. *Int. J. Pattern Recognit. Artif. Intell.* 11:1317–43
65. Dupuis P, Grenander U, Miller MI. 1998. Variational problems on flows of diffeomorphisms for image matching. *Q. App. Math.* 56:587–600
66. Van Essen DC, Drury H, Joshi S, Miller MI. 1998. Functional and structural mapping of human cerebral cortex: solutions are in the surfaces. *Proc. Natl. Acad. Sci. USA* 95:788–95
67. Bakircioglu M, Grenander U, Khaneja N, Miller MI. 1998. Curve matching on brain surfaces using frenet distances. *Human Brain Mapp.* 6(5):329–32

68. Younes L. 1998. Computable elastic distances between shapes. *SIAM J. Appl. Math.* 58:565–86
69. Joshi SC, Miller MI. 2000. Landmark matching via large deformation diffeomorphisms. *IEEE Trans. Image Process.* 9:1357–70
70. Bakircioglu M, Joshi SC, Miller MI. 1999. Landmark matching on brain surfaces via large deformation diffeomorphisms on the sphere. *Proc. SPIE Med. Imaging Image Process.* 3661:710–15
71. Miller MI, Younes L. 2001. Group actions, homeomorphisms, and matching: a general framework. *Int. J. Comput. Vis.* 41:61–84
72. Miller MI, Massie A, Ratnanather JT, Botteron KN, Csernansky J. 2000. Bayesian construction of geometrically based cortical thickness metrics. *NeuroImage* 12:676–87
73. Ratnanather JT, Botteron KN, Nishino T, Massie AB, Lal RM, et al. 2001. Validating cortical surface analysis of medial prefrontal cortex. *NeuroImage* 14:1058–69
74. Joshi M, Cui J, Doolittle K, Joshi S, Van Essen D, et al. 1999. Brain segmentation and the generation of cortical surfaces. *NeuroImage* 9:461–76
75. Miller MI, Khaneja N, Grenander U. 1998. Dynamic programming generation of curves on brain surfaces. *Pattern Anal. Mach. Intell.* 20(10):1260–64
76. Trouvé A. 1998. Diffeomorphisms groups and pattern matching in image analysis. *Int. J. Comput. Vis.* 28:213–21
76a. Trouvé A,Younes L. 2002. *Local Analysis on a Shape Manifold. Univ. Paris 13 Tech. Rep.*
77. Sandor T, Jolesz F, Tieman J, Kikinis R, LeMay M, Albert M. 1991. Extraction of morphometric information from dual echo magnetic resonance brain images. In *Visual Communications and Image Processing '90: SPIE Proceedings*, 1360:665–75. Bellingham, WA: SPIE
78. McCarley RW, Shenton ME, O'Donnell BF, Faux SF, Kikinis R, et al. 1993. Auditory p300 abnormalities and left posterior superior temporal gyrus volume reduction in schizophrenia. *Arch. Gen. Psychiatry* 50:190–97
79. Menon RR, Barta PE, Aylward EH, Richards SS, Vaughn DD, et al. 1995. Posterior superior temporal gyrus in schizophrenia: gray matter changes and clinical correlates. *Schizophr. Res.* 16:127–35
80. Iosifescu DV, Shenton ME, Warfield SK, Kikinis R, Dengler J, et al. 1997. An automated registration algorithm for measuring MRI subcortical brain structures. *NeuroImage* 6:13–25
81. Warfield SK, Jolesz FA, Kikinis R. 1998. A high performance computing approach to the registration of medical imaging data. *Parallel Comput.* 24: 1345–68
82. Hata N, Nabavi A, Wells WM III, Warfield SK, Kikinis R, et al. 2000. Three-dimensional optical flow method for measurement of volumetric brain deformation from intraoperative MR images. *J. Comp. Assist. Tomog.* 24(4):531–38
83. Davatzikos C. 1996. Spatial normalization of 3-D brain images using deformable models. *J. Comp. Assist. Tomog.* 20(4):656–65
84. Davatzikos C, Vaillant M, Resnick SM, Prince JL, Letovsky S, Bryan RN. 1996. A computerized approach for morphological analysis of the corpus callosum. *J. Comp. Assist. Tomog.* 29(1):88–97
85. Kyriacou SK, Davatzikos C, Zinreich SJ, Bryan RN. 1999. Nonlinear elastic registration of brain images with tumor pathology using a biomechanical model. *IEEE Trans. Med. Imag.* 18:580–92
86. Davatzikos C. 1997. Spatial transformation and registration of brain images using elastically deformable models. *Comp. Vis. Image Underst.* 66(2):207–22

87. Davatzikos C. 2001. Measuring biological shape using geometry-based shape transformations. *J. Image Vis. Comp.* 19:63–74
88. Davatzikos C, Shen D, Mohamed A, Kyriacou S. 2001. A framework for predictive modeling of anatomical deformations. *IEEE Trans. Med. Imaging* 20: 836–43
89. Vaillant M, Davatzikos C. 1997. Finding parametric representations of the cortical sulci using an active contour model. *Med. Image Anal.* 1(4):295–315
90. Shen D, Herskovits EH, Davatzikos C. 2001. An adaptive focus statistical shape model for segmentation and shape modeling of 3D brain structures. *IEEE Trans. Med. Imaging* 20:257–71
91. Xu C, Pham DL, Rettmann ME, Yu DN, Prince JL. 1999. Reconstruction of the human cerebral cortex from magnetic resonance images. *IEEE Trans. Med. Imaging* 18(6):467–80
92. Pham DL, Xu C, Prince JL. 2000. Current methods in medical image segmentation. *Annu. Rev. Biomed. Eng.* 2:315–37
92a. Sapiro G. 2001. *Geometric Partial Differential Equations and Image Analysis.* Cambridge, UK: Cambridge Univ. Press. 385 pp.
92b. Bartesaghi A, Sapiro G. 2001. A system for the generation of curves on 3D brain images. *Human Brain Mapp.* 14:1–15
92c. Teo P, Sapiro G, Wandell B. 1997. Creating connected representations of cortical gray matter for functional MRI visualization. *IEEE Trans. Med Imaging* 16:852–63
93. Hurdal MK, Bowers PL, Stephenson K, Sumners DL, Rehm K, et al. 1999. Quasi-conformally flat mapping the human cerebellum. In *Lecture Notes in Computer Science*, ed. C Taylor, A Colchester, pp. 279–86. Berlin: Springer-Verlag
94. Toga AW, Thompson P, Payne BA. 1996. Modeling morphometric changes of the brain during development. In *Development Neuroimaging: Mapping the Development of Brain and Behavior*, ed. RW Thatcher, G Reid Lyon, J Rumsey, N Krasnegor, pp. 15–27. San Diego: Academic
95. Toga AW, Thompson PM. 1999. An introduction to brain warping. See Ref. 123, pp. 1–26
96. Thompson PM, Toga AW. 1999. Anatomically driven strategies for high-dimensional brain image warping and pathology detection. See Ref. 123, pp. 311–36
97. Thompson PM, Giedd JN, Woods RP, MacDonald D, Evans AC, Toga AW. 2000. Growth patterns in the developing brain detected by using continuum mechanical tensor maps. *Nature* 404:190–93
98. Thompson PM, Vidal C, Giedd JN, Gochman P, Blumenthal J, et al. 2001. Mapping adolescent brain change reveals dynamic wave of accelerated gray matter loss in very early-onset schizophrenia. *Proc. Natl. Acad. Sci. USA* 98:11650–55
99. Van Essen DC, Drury H. 1997. Structural and functional analyses of human cerebral cortex using a surface-based atlas. *J. Neurosci.* 17:7079–102
100. Van Essen DC, Lewis JW, Drury HA, Hadjikhani NA, Tootell RL, et al. 2001. Mapping visual cortex in monkeys and humans using surface-based atlases. *Vis. Res.* 41:1359–78
101. Drury HA, Van Essen DC, Anderson CH, Lee CH, Coogan TA, Lewis JW. 1996. Computerized mappings of the cerebral cortex: a multiresolution flattening method and a surface-based coordinate system. *J. Cogn. Neurosci.* 8:1–28
101a. Wandell B. 1999. Computational neuroimaging of human visual cortex. *Annu. Rev. Neurosci.* 22:145–79
101b. Wandell B, Chial S, Backus B. 2000. Visualization and measurement of the

cortical surface. *J. Cogn. Neurosci.* 12: 739–52
102. Terzopoulos D. 1984. *Multiresolution computation of visible-surface representations*. PhD Thesis, Massachusetts Institute of Technology, Boston, MA
103. Terzopoulos D, Waters K. 1990. Physically-based facial modelling, analysis, and animation. *J. Vis. Comput. Animat.* 1:73–80
104. Carlbom I, Terzopoulos D, Harris K. 1994. Computer-assisted registration, segmentation, and 3D reconstruction from images of neuronal tissue sections. *IEEE Trans. Med. Imaging* 13(2):351–62
105. Terzopoulos D, Metaxas D. 1991. Dynamic 3D models with local and global deformations: deformable superquadrics. *IEEE Trans. Patterns Anal. Mach. Intell.* 13:703–14
106. Pentland A, Sclaroff S. 1991. Closed-form solutions for physically based shape modeling and recognition. *IEEE Trans. Pattern Anal. Mach. Intell.* 13(7): 715–29
107. Martin J, Pentland A, Sclaroff S, Kikinis R. 1998. Characterization of neuropathological shapes deformation. *IEEE Trans. Pattern Anal. Mach. Intell.* 30:97–112
108. Sclaroff S, Liu L. 2001. Deformable shape detection and description via model-based region grouping. *IEEE Trans. Pattern Anal. Mach. Intell.* 23: 475–89
109. Cootes TF, Taylor CJ, Cooper DH, Graham J. 1995. Active shape models—their training and application. *Comp. Vis. Image Underst.* 61(1):38–59
110. Hill A, Cootes TF, Taylor CJ. 1996. Active shape models and the shape approximation problem. *Image Vis. Comput.* 14:601–8
111. Cootes TF, Edwards GJ, Taylor CJ. 2001. Active appearance models. *IEEE Trans. Pattern Anal. Mach. Intell.* 23:681–85
112. Mumford D. 1998. Pattern theory and vision. In *Questions Matheématiques En Traitement Du Signal et de L'Image*, Chapter 3, pp. 7–13. Paris: Institut Henri Poincaré
113. Boothby WM. 1986. *An Introduction to Differentiable Manifolds and Riemannian Geometry*. San Diego: Academic
114. Marsden JE, Ratiu T. 1999. *Introduction to Mechanics and Symmetry*. New York: Springer-Verlag
115. Kendall DG. 1984. Shape manifolds, procrustean metrics and complex projective spaces. *Bull. London Math. Soc.* 16:81–121
116. Giovanni S. 1959. *Orthogonal Functions*. New York: Wiley
117. Corbetta M, Akbudak E, Conturo TE, Snyder AZ, Ollinger JM, et al. 1998. A common network of functional areas for attention and eye movements. *Neuron* 21(4):761–73
118. Amit Y, Piccioni M. 1991. A nonhomogeneous Markov process for the estimation of Gaussian random fields with nonlinear observations. *Ann. Probab.* 19:1664–78
118a. Amit Y, Grenander U, Piccioni M. 1991. Structural image restoration through deformable templates. *J. Am. Stat. Assoc.* 86:376–87
119. Csernansky JG, Joshi SC, Wang L, Gado M, Miller JP, et al. 1998. Hippocampal morphometry in schizophrenia by high dimensional brain mapping. *Proc. Natl. Acad. Sci. USA* 95:11406–11
120. Csernansky JG, Wang L, Joshi S, Philip Miller J, Gado M, et al. 2000. Early DAT is distinguished from aging by high dimensional mapping of the hippocampus. *Neurology* 55:1636–43
121. Wang L, Joshi SC, Miller MI, Csernansky JG. 2001. Statistical analysis of hippocampal asymmetry in schizophrenia. *NeuroImage* 14:531–45
122. Anderson TW. 1984. *An Introduction to Multivariate Statistical Analysis*. New York: Wiley
123. Toga AW, ed. 1999. *Brain Warping*. San Diego: Academic. 385 pp.

APPENDIX

Proof of Theorem 3.1: To derive Euler-Lagrange equations for the velocity examine perturbations on the group elements and velocity fields, $g \to g + \epsilon\eta$, $v \to v + \epsilon\psi$. For exact correspondence of the group elements, $\eta(0) = \eta(1) = 0$, as depicted in panel 2 of Figure 1. For inexact image matching, only $\eta(0) = 0$ with $\eta(x, t) = 0$, $\forall x \in \partial X$, $\psi(x, t) = 0$, $\forall x \in \partial X$. If η is a perturbation of g, define the *Gateaux differential* of $E(v_g) : \mathcal{G} \to \mathbb{R}^+$ in the direction η to be the limit, as the perturbation tends to 0. Also if ψ is a perturbation of v, define the *Gateaux differential* of $E(g_v) : \mathcal{V} \to \mathbb{R}^+$ in the direction ψ to be the limit, as the perturbation tends to 0.

Lemma A.1 *The variations of the velocity and group element via ψ, η are given by*

$$\begin{aligned}\psi(x,t) = \partial_\eta v_g(x,t) &= \lim_{\epsilon\to 0}\frac{1}{\epsilon}(v_{g+\epsilon\eta}(x,t) - v_g(x,t)) \\ &= \frac{d}{dt}\eta(g^{-1}(x,t),t) - Dv_g(x,t)\eta(g^{-1}(x,t),t) \qquad (25)\end{aligned}$$

$$\begin{aligned}\eta(x,t) = \partial_\psi g_v(x,t) &= \lim_{\epsilon\to 0}\frac{1}{\epsilon}(g_{v+\epsilon\psi}(x,t) - g_v(x,t)) \\ &= Dg_v(x,t)\int_0^t Dg_v(x,u)^{-1}\psi(g_v(x,u),u)\,du. \qquad (26)\end{aligned}$$

Proof of Lemma: Defining the notation $x \simeq y$ to mean $\lim_{\epsilon\to 0}\frac{x-y}{\epsilon} = 0$, then

$$\begin{aligned}\frac{d}{dt}(g+\epsilon\eta)(x,t) &= v_g(g(x,t),t) + \epsilon\frac{d}{dt}\eta(x,t) \\ &= v_{g+\epsilon\eta}(g(x,t)+\epsilon\eta(x,t),t) \qquad (27)\end{aligned}$$

$$\overset{(a)}{\simeq} v_g(g(x,t),t) + \epsilon Dv_g(g(x,t),t)\eta(x,t) + \epsilon\partial_\eta v_g(g(x,t),t), \qquad (28)$$

with (a) following from the definition of $\partial_\eta v_g$, the total derivative and the $o(\epsilon)$ equality. Equating Equations 27 and 28 gives the first result of Equation 25. Equation 26 follows from the linearity of η given ψ fixed in Equation 25:

$$\begin{aligned}\frac{\partial}{\partial t}\eta(x,t) &= Dv(g(x,t),t)\eta(x,t) + \psi(g(x,t),t) \\ &= \frac{\partial}{\partial t}Dg(x,t)(Dg(x,t))^{-1}\eta(x,t) + \psi(g(x,t),t) \qquad (29)\end{aligned}$$

since

$$\frac{\partial}{\partial t}Dg(x,t) = Dv(g(x,t),t)Dg(x,t). \qquad (30)$$

Then η in Equation 26 satisfies the derivative Equation 29, completing the proof of the Lemma.

Consider the energy $E(v_g)$ defined for all time-dependent diffeomorphisms $g(\cdot, t)$ solving $\frac{dg}{dt} = v(g, t)$. Now evaluating the variation of $E(v_g) = \int_0^1 E_{v_g}(t)\,dt$ with respect to perturbations $g \to g + \epsilon\eta$ gives

$$\partial_\eta E(v_g) = \lim_{\epsilon\to 0} \frac{1}{\epsilon}(E(v_{g+\epsilon\eta}) - E(v_g))$$
$$\stackrel{(a)}{=} \int_0^1 \langle \nabla_v E(\cdot, t), \frac{d}{dt}\eta(g^{-1}(\cdot, t), t) - Dv(\cdot, t)\eta(g^{-1}(\cdot, t), t))\rangle\, dt \quad (31)$$

$$\stackrel{(b)}{=} \langle \nabla_v E(\cdot, t), \eta(g^{-1}(\cdot, t), t)\rangle|_0^1$$
$$- \int_0^1 \left\langle \frac{d}{dt}(|Dg(\cdot, t)|\nabla_v E(g(\cdot, t), t)), \eta(\cdot, t)\right\rangle dt$$
$$- \int_0^1 \langle |Dg(\cdot, t)|\nabla_v E(g(\cdot, t), t), Dv(g(\cdot, t), t)\eta(\cdot, t)\rangle\, dt, \quad (32)$$

with (a) coming from Equation 25, and (b) the change of variables $y = g(x, t)$, with integration by parts eliminating the time derivative of η. The first term is the boundary term which is zero for exact matching. This gives the terms in the inner product forming the Euler-Lagrange functional variation:

$$-\frac{d}{dt}(\nabla_v E(g(x, t), t)|Dg(x, t)|) - (Dv(g(x, t), t))^t \nabla_v E(g(x, t), t)|Dg(x, t)| \quad (33)$$

$$= -\left(\frac{\partial}{\partial t}\nabla_v E\right)(g(x, t), t)|Dg(x, t)| - (D\nabla_v E)(g(x, t), t)v(g(x, t), t)|Dg(x, t)|$$
$$- \frac{\partial}{\partial t}(\log|Dg(x, t)|)\nabla_v E(g(x, t), t)|Dg(x, t)|$$
$$- (Dv(g(x, t), t))^t \nabla_v E(g(x, t), t)|Dg(x, t)|. \quad (34)$$

Now the identity for the derivative of the log-determinant is given by $\log|A + \epsilon B| = \log|A| + \epsilon$ trace $A^{-1}B + o(\epsilon)$, and the time derivative of the Jacobian $\frac{\partial}{\partial t}Dg(x, t)$ is given by Equation 30 so that

$$\frac{\partial}{\partial t}\log|Dg(x, t)| = \text{trace}\,((Dg(x, t))^{-1}Dv(g(x, t), t)Dg(x, t))$$
$$= \text{trace}\, Dv(g(x, t), t) = \text{div}\, v(g(x, t), t). \quad (35)$$

Substituting along with $y = g(x, t)$ into Equation 34 gives the Euler-Lagrange equation (Equation 4) completing the first part of the proof.

Proof of Theorem 3.3: Define the energy $E(g_v, J) = \int_0^1 (\|v(t)\|_L^2 + \|\frac{\partial J}{\partial t}(t) + \nabla J^t(t)v(t)\|^2)\,dt$. This has to be minimized jointly in v and J. The gradient in v is given by $\nabla_v E = 2L^\dagger L v + 2(\frac{\partial}{\partial t}J(t) + \nabla J^t(t)v(t))\nabla J(t)$. The nonboundary term for the perturbation is identical to the above, giving Equation 4. The boundary

condition at $t=1$ applies since $g(1)$ is free at the endpoint, so the value of the perturbation $\eta(\cdot, 1)$ is nonzero, and the boundary term must be taken into account from Equation 32, giving $\langle \nabla_v E(1), \eta(g^{-1}(1), 1)\rangle = 0$ so that $\nabla_v E(1) = 0$. The variation in J follows by introducing $Z = \frac{\partial J}{\partial t} + \nabla J^t v$, and computing the perturbation by ϕ with v fixed:

$$\lim_{\epsilon\to 0} \frac{E(g_v, J+\epsilon\phi) - E(g_v, J)}{\epsilon}$$

$$= 2\int_0^1 \left\langle Z(t), \frac{\partial}{\partial t}\phi(t) + \nabla\phi^t(t)v(t)\right\rangle dt$$

$$= -2\int_0^1 \left\langle \frac{\partial}{\partial t} Z(t), \phi(t)\right\rangle dt - 2\int_0^1 \langle \nabla(Z(t)v(t)), \phi(t)\rangle\, dt.$$

Proof of Inexact Image Matching Theorem 4.1: To compute the boundary term Equation 11 which holds for inexact matching at the endpoint $t=1$, the variation of the inverse map $\partial_\eta g^{-1}$ in a perturbation is required:

$$\begin{aligned} y &= (g+\epsilon\eta)((g+\epsilon\eta)^{-1}(y,t),t) \\ &\simeq g((g+\epsilon\eta)^{-1}(y,t),t) + \epsilon\eta((g+\epsilon\eta)^{-1}(y,t),t) \\ &= y + Dg(g^{-1}(y,t))((g+\epsilon\eta)^{-1}(y,t) - g^{-1}(y,t)) + \epsilon\eta(g^{-1}(y,t),t), \end{aligned}$$

implying

$$\lim_{\epsilon\to 0} \frac{1}{\epsilon}((g+\epsilon\eta)^{-1}(y,t) - g^{-1}(y,t)) \overset{(a)}{=} -Dg^{-1}(y,t)\eta(g^{-1}(y,t),t), \quad (36)$$

with (a) from $Dg_v^{-1}(y,t) = (Dg_v(g_v^{-1}(y,t),t))^{-1}$. The variation of the second matching term becomes

$$\partial_\eta \|I_1 - I_0(g^{-1})\|^2 = -2\big\langle I_1 - I_0(g^{-1}(1)), \nabla I_0^t(g^{-1}(1))\partial_\eta g^{-1}(1)\big\rangle, \quad (37)$$

$$\overset{(a)}{=} 2\big\langle I_1 - I_0(g^{-1}(1)), \nabla I_0^t(g^{-1}(1))Dg^{-1}(1)\eta(g^{-1}(1),1)\big\rangle, \quad (38)$$

$$\overset{(b)}{=} 2\langle I_1 - I_0(g^{-1}(1))D(I_0(g^{-1}(1)))^t, \eta(g^{-1}(1),1)\rangle, \quad (39)$$

with (a) using Equation 36 and (b) collecting terms $D(I_0(g^{-1}(y,1))) = \nabla I_0^t(g^{-1}(y,1))\, Dg^{-1}(y,1)$. At $t=1$ with $g^{-1}(1)$ free the boundary term Equation 32 is nonzero; adding it to Equation 39 gives Equation 11.

Proof of Space-Time Growth Theorem 4.2: Substitution of $y = g(x,t)$ in Equation 34 gives the variation of the $\|v(t)\|_L^2$ to be:

$$-\int_0^1 \left\langle \frac{\partial}{\partial t}\nabla_v E_v(\cdot,t) + (Dv(\cdot,t))^t \nabla_v E_v(\cdot,t) + (D\nabla_v E_v(\cdot,t))v(\cdot,t) \right.$$

$$\left. + \operatorname{div} v(\cdot,t)\nabla_v E_v(\cdot,t), \eta(g^{-1}(t),t)\right\rangle dt. \quad (40)$$

The variation of the second term under the perturbation of g by η follows from using Equation 36:

$$-2\int_0^1 \left\langle (I_1(t) - I_0(g^{-1}(t)), \nabla I_0^t(g^{-1}(t))\partial_\eta g^{-1}(t)\right\rangle dt \tag{41}$$

$$= 2\int_0^1 \left\langle (I_1(t) - I_0(g^{-1}((t), t), \nabla I_0^t(g^{-1}(t))Dg^{-1}(t)\eta(g^{-1}(t), t)\right\rangle dt \tag{42}$$

$$\overset{(a)}{=} 2\int_0^1 \langle (I_1(t) - I_0(g^{-1}(t))D(I_0(g^{-1}(t)))^t, \eta(g^{-1}(t), t)\rangle\, dt, \tag{43}$$

with (a) writing $D(I_0(g^{-1}(t))) = \nabla I_0^t(g^{-1}(t))Dg^{-1}(t)$. Collecting the two components of the gradient term from Equations 40 and 43 gives the proof.

Proof of Theorem 6.2: Define normalized landmarks $\gamma(x_n,\ t) = \frac{g(x_n,t)-\bar{g}(t)}{\sigma(g(t))}$, $g(x_n, t) = \sigma(g(t))\,\gamma(x_n, t) + \bar{g}(t)$, then

$$\frac{\partial g}{\partial t}(x_n, t) = \frac{d\sigma(g(t))}{dt}\gamma(x_n, t) + \sigma(g(t))\frac{\partial \gamma}{\partial t}(x_n, t) + \frac{d\bar{g}}{dt}, \tag{44}$$

implying $\int_0^1 \|\frac{\partial g(t)}{\partial t}\|^2_{Q(g(t))}\, dt$ equals

$$\begin{aligned}
&\sum_{n=1}^N \Bigg(\int_0^1 \frac{1}{\sigma^2(g(t))}\left(\frac{d\sigma(g(t)}{dt}\right)^2 |\gamma(x_n, t)|^2\, dt \\
&+ \int_0^1 \frac{1}{\sigma^2(g(t))}\frac{d\bar{g}^2}{dt}\, dt + \int_0^1 \left\| \frac{\partial \gamma}{\partial t}(x_n, t)\right\|^2 dt \\
&+ 2\int_0^1 \frac{1}{\sigma(g(t))}\frac{d\sigma(g(t)}{dt}\gamma(x_n, t)\frac{d\gamma(x_n, t)}{dt} + 2\int_0^1 \frac{1}{\sigma(g(t))^2}\frac{d\bar{g}(t)}{dt}\gamma(x_n, t)\, dt \\
&+ 2\int_0^1 \frac{1}{\sigma(g(t))}\bar{g}(t)\sum_{n=1}^N \frac{d\gamma(x_n, t)}{dt}\, dt \Bigg) \\
&\overset{(a)}{=} \int_0^1 \frac{1}{\sigma^2(g(t))}\left(\frac{d\sigma(g(t)}{dt}\right)^2 dt + N\int_0^1 \frac{1}{\sigma^2(g(t))}\frac{d\bar{g}^2}{dt}\, dt \\
&+ \int_0^1 \sum_{n=1}^N \left\| \frac{d\gamma}{dt}(x_n, t)\right\|^2 dt,
\end{aligned} \tag{45}$$

with (a) following from $\|\gamma(t)\|^2 = 1$, implying the 4th term $\frac{d}{dt}\|\gamma(t)\|^2 = 0$, the 5th term has mean zero, and the final term is the derivative of the mean, which is zero. Denote by $\rho_0((\sigma(g(0)),\ \bar{g}(0)),\ (\sigma(g(1)),\ \bar{g}(1)))^2$ the minimum of the first two terms; the minimum of the last term can be explicitly computed (because $(\gamma(., x_1), \ldots, \gamma(\cdot, x_N))$ and belongs to a sphere of dimension $N-2$ and is given by

the length of the great circle in the sphere which connects the extremities of the path, namely $(\arccos \sum_{n=1}^{N} \langle \gamma(0, x_n), \gamma(1, x_n) \rangle)^2$ so,

$$\rho(I_N, I'_N)^2 = \rho_0((\sigma(g(0)), \bar{g}(0)), (\sigma(g(1)), \bar{g}(1)))^2 + \left(\arccos \sum_{n=1}^{N} \langle \gamma(0, x_n), \gamma(1, x_n) \rangle_{\mathbb{R}^d} \right)^2 . \quad (46)$$

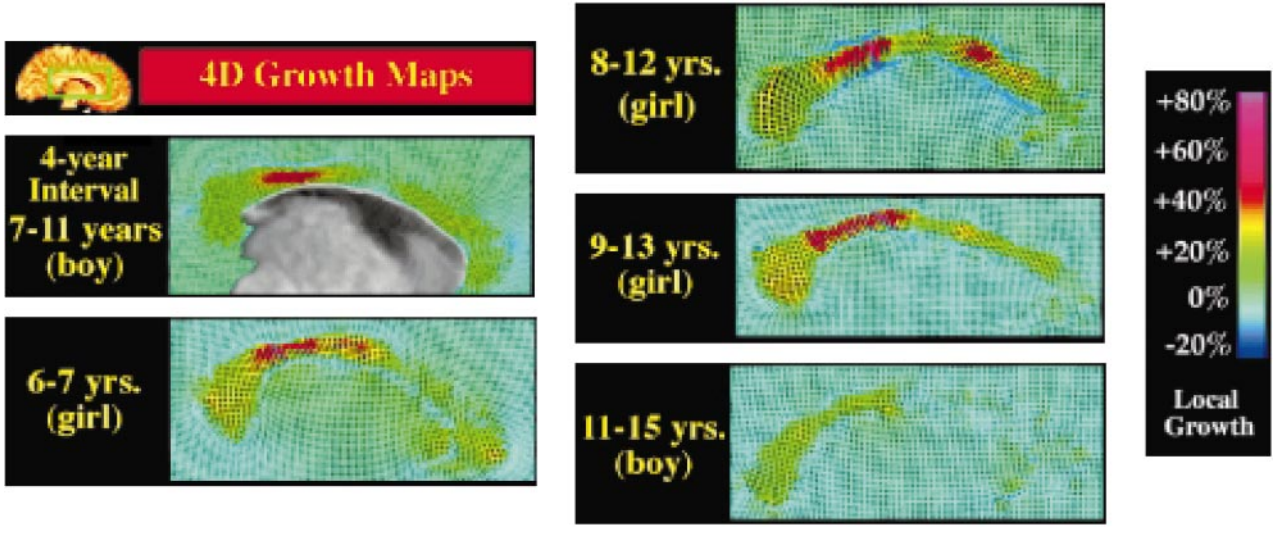

Figure 6 Deformation maps showing growth in the corpus callosum area from the Toga laboratory at UCLA. Maps based on scanning the children at various stages with deformation fields applied to the regular grid overlaid on the earliest anatomy. The Jacobian determinant, whose values are coded in color on the deformed grid, shows the local growth rate (*red colors*, rapid growth). Fastest growth is found consistently, across ages 7–13, in the isthmus, a region of the corpus callosum that carries fibers to areas of the cerebral cortex that support language function, and areas of the temporo-parietal cortex that support associative and mathematical thinking. Results taken from Thompson et al. (97).

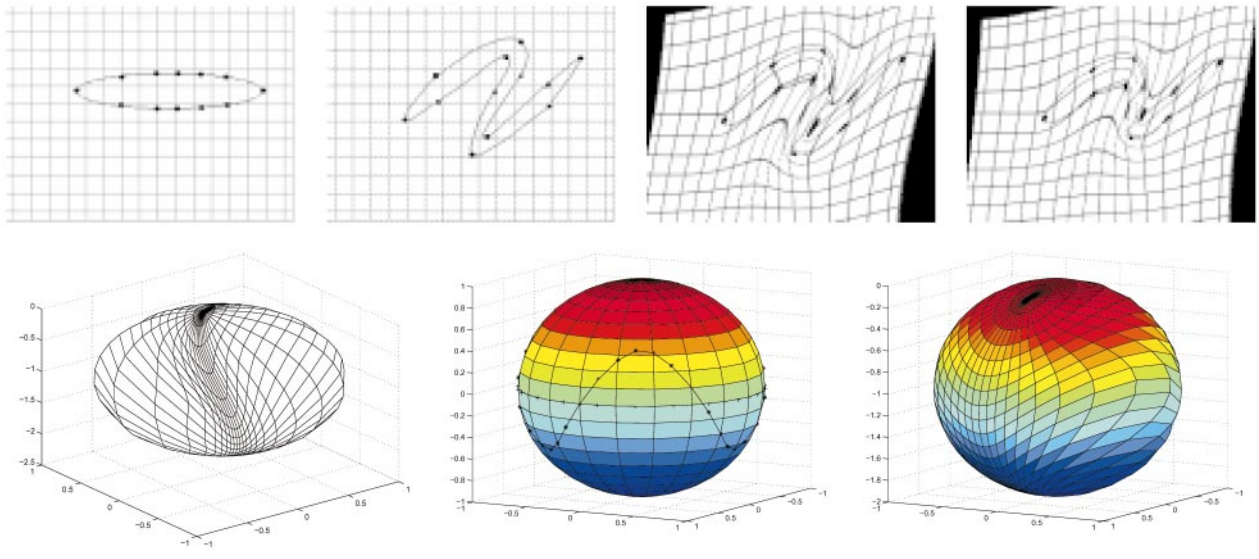

Figure 8 (*Top row*) Panels 1–2 show the two test patterns and the matching (panels 3–4) using variances of $\sigma^2 = 0.1{,}10$, respectively. Results from (69). (*Bottom row*) Panel 5 shows spherical deformations driven by three landmarks along the longitude line $\theta = \pi/3$ mapped to the corresponding points along the line $\theta = \pi/4$. Notice the contraction of the longitude lines between $\theta = \pi/3$ and $\theta = \pi/4$. Panel 6 shows a sinusoid of landmarks on the sphere with the resulting deformation shown in panel 7. Notice the dramatic deformation of spherical coordinates. Results taken from Bakircioglu et al. (70).

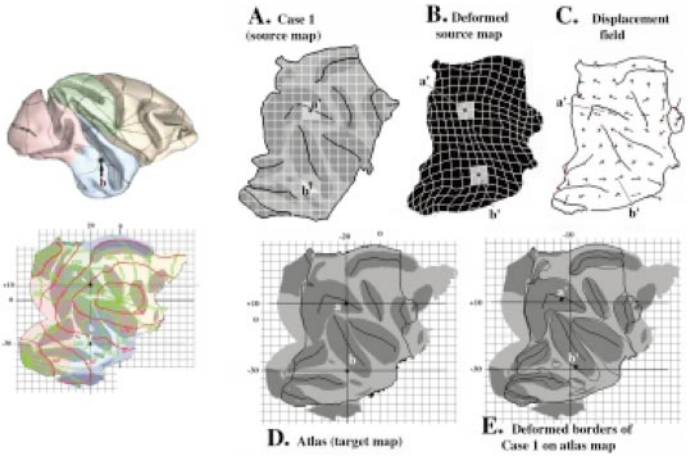

Figure 9 Two columns show the Van Essen surface-based atlas of macaque visual cortex. Left column shows the macaque atlas (*top row*) and flattened version (*bottom row*). Panel *A* shows the flat map. Shading indicates cortical geography, black lines indicate the landmark contours used to constrain the deformation (along sulcal fundi and along the map perimeter). Panel *B* shows the pattern of grid lines after deformation into register with the target atlas map in panel *D*. Panel *C* shows the vector field for selected grid points (at intervals of 10 map-mm). Arrow bases indicate grid positions in the source map, and arrow tips indicate the location of grid points in the deformed source map. Panel *D* shows the map of geography (*shading*) and target registration contours (*black lines*) on the atlas map. Panel *E* shows contours from the deformed source map (*black lines*). Results from (100).

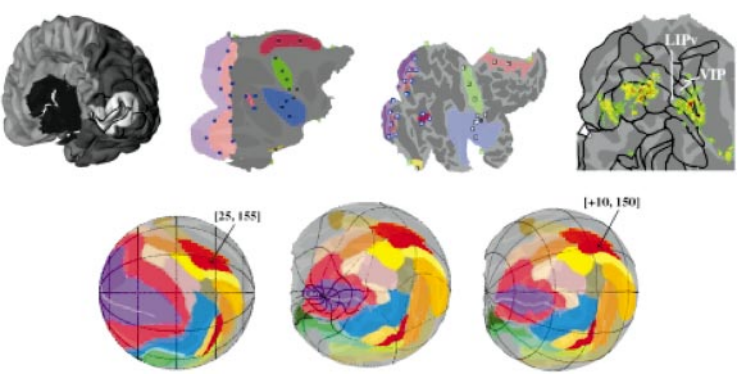

Figure 10 (*Top row*) Panel 1 shows 3-D Visible Human Male, panel 2 shows the landmarks on macaque flat maps, panel 3 shows the landmarks on the human flat maps, and panel 4 shows the boundaries of deformed macaque visual areas (*black lines*) superimposed on the fMRI activation pattern from an attentional task from Corbetta et al. (117) after deformation to the Visible Man atlas. (*Bottom row*) Panel 5 shows the spherical map of the macaque visual cortex. Panel 6 shows the spherical map of the deformed macaque visual areas, along with the deformed latitude and longitude isocontours. Panel 7 shows the deformed macaque visual areas with the latitude and longitude lines of the Visible Human spherical map. Results taken from Van Essen et al. (100).

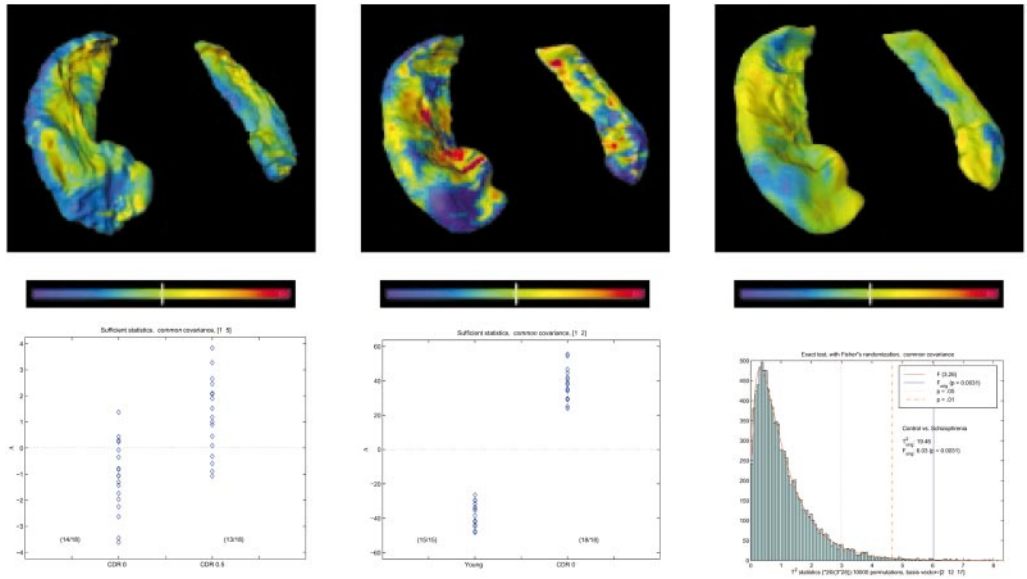

Figure 11 Top row shows difference of hippocampal surface patterns between the control and AD (*left*), normal aging (*middle*), and schizophrenia (*right*) groups visualized as *z*-scores on the mean surface (*top view*). Inward surface deformations are visualized in colder colors, outward in warmer colors, undeformed areas in neutral yellow to green colors. The left and middle panels of the bottom row show the log-likelihood ratio statistic from jacknifing based on principal component analysis of shape difference. Panel 4 shows the difference of hippocampal surface patterns between the elderly and AD groups based on the principal component analysis of shape differences for basis functions {1,5}. Multivariate ANOVA indicates between-group asymmetry: p = .0002 ($F = 11.4$, $df = 2,33$). Panel 5 shows the differences between the younger and the elderly groups based on principal components {1,2}. ANOVA again indicates significant between-group asymmetry: p < .0001 ($F = 348$, $df = 2,30$). Panel 6 shows Joshi's results (69) on distribution free testing based on the recommendations of Drs. Fred Bookstein and Stuart Geman, demonstrating the Gaussian model is valid.